Anomalous Change in the de Haas-van Alphen Oscillations of $CeCoIn_5$ at Ultralow Temperatures

H. Shishido, Y. Yanase, and M. Yamashita

A very strange quantum behavior is found in a strongly-correlated superconductor at unprecedented ultralow temperatures [1]. The heavy-fermion compound $CeCoIn_5$ is the celebrated, one of the most-studied *d*-wave superconductor [2]. Its unconventional superconductivity has been thought to be arisen by quantum fluctuations near the magnetically ordered state. However, in spite of many efforts, the ordered state has yet to be discovered.

By using our home-made nuclear-demagnetization cryostat at ISSP, we performed the de Haas-van Alphen (dHvA) measurements of $CeCoIn_5$ down to 2 mK. In a normal metal, a dHvA amplitude increases with a lowering temperature in accordance with the Lifshitz-Kosevich (LK) formula. However, in $CeCoIn_5$, we unexpectedly find that the dHvA amplitudes deviate from the LK formula and show an anomalous decrease with a shift of the dHvA frequencies below a transition temperature T_n (Fig. 1). This anomalous change suggests that the long-presumed ordered state is finally discovered at ultralow temperatures unreachable for conventional cryostats.

The revised H–T phase diagram of $CeCoIn_5$ (Fig. 2(a)) reveals that the field-induced AFM phase is located at the boundary of the unconventional superconductivity. Given that the field-induced phase is observed at very low temperature, the H–T phase diagram of $CeCoIn_5$ at ambient pressure may be considered to be a cross section at the vicinity of the AFM QCP in the H–T–x phase diagram (Fig. 2(b)) obtained by the pressure dependence of the H–T phase diagram of $CeRhIn_5$ [3]. Thus, our study shows that $CeCoIn_5$ is a prominent superconductor where the interplay of unconventional superconductivity, magnetic order, and non-Fermi liquid behaviors near the QCP can be studied without the ambiguity caused by the application of pressure or chemical doping.

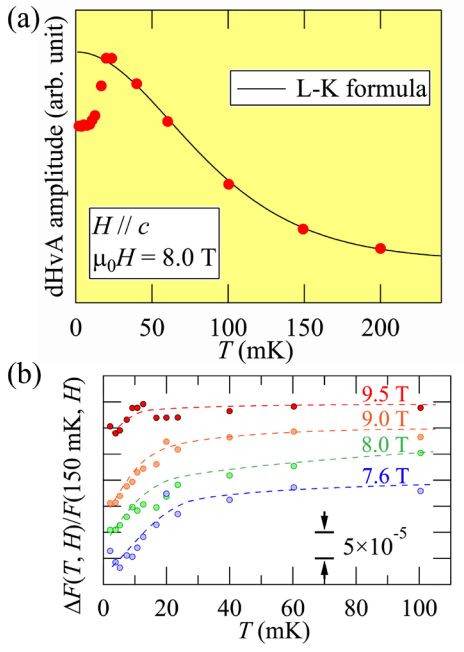

Fig. 1. (a) The temperature dependence of the dHvA amplitude of α_3 branch of $CeCoIn_5$. The solid line shows the fit of the data from the standard Lifshitz-Kosevich formula. (b) The temperature dependence of the normalized shift of the dHvA frequency $\Delta F(T, H) / F(150\ \mathrm{mK}, H)$ of α_3 branch. The data are shifted for clarity. The dashed lines are guides for the eye.

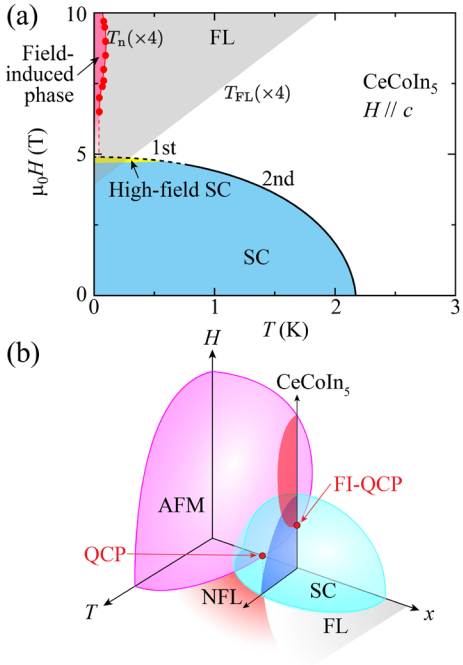

Fig. 2. (a) The H-T phase diagram of $CeCoIn_5$. Field-induced phase found by our measurements (pink), the Fermi liquid (FL) region (gray), the superconducting (SC) phase (blue), and the high-field SC phase (yellow) are shown. Both T_n (the red circles) and T_{FL} are multiplied by 4 for clarity. (b) A schematic H–T–x phase diagram near the AFM QCP, where x denotes pressure or chemical substitution. The cross section corresponds to the H–T phase diagram of $CeCoIn_5$, in which a presumed field-induced QCP (FI QCP) is also shown at the intersection with the AFM boundary.

We also find that the transition temperature T_n depends on field only weakly for 7–10 T even though the Zeeman energy at 10 T is about 3 orders of magnitude larger than k_BT_n. This field dependence implies that AFM order is enhanced by suppressing the critical spin fluctuations in the vicinity of the AFM QCP in high fields, which gives rise to the weak field dependence of T_n, as supported by the FLEX calculation [4].

Future studies for the detailed structure of the newly-found state would reveal the origin of the unconventional superconductivity in the proximity of a magnetically ordered state. As demonstrated by this study, we believe that the development of the ultralow-temperature measurements

has extensive potential to shed a new light on unexplored phenomena.

References
[1] H. Shishido *et al.*, Phys. Rev. Lett. **120**, 177201 (2018).
[2] K. Izawa *et al.*, Phys. Rev. Lett. **87**, 057002 (2001).
[3] J. L. Sarrao and J. D. Thompson, J. Phys. Soc. Jpn. **76**, 051013 (2007).
[4] Y. Yanase, J. Phys. Soc. Jpn. **77**, 063705 (2008).

Authors
H. Shishido[a,b], S. Yamada, K. Sugii, M. Shimozawa, Y. Yanase[c], and M. Yamashita
[a]Osaka Prefecture University
[b]Institute for Nanofabrication Research, Osaka Prefecture University
[c]Kyoto University

Spin Current Noise of the Spin Seebeck Effect and Spin Pumping

M. Matsuo and T. Kato

In the research field of mesoscopic physics, current noise measurement is an important tool to obtain useful information on electronic transport such as determination of the effective charge, evaluation of electron entanglement, and even spin accumulation. In the research field of spintronics, the pure spin current induced by, e.g., spin pumping and spin Seebeck effect (see the upper two schematic pictures in Fig. 1), is a central research subject. Recently, the noise of this pure spin current has measured by using the inverse spin Hall effect [1]. Although the noise of the pure spin current is expected to have useful information, its theoretical study has, however, been overlooked for a long time, and has just started recently in a few papers [2].

In our study [3], we considered a normal metal(NM)/ ferromagnetic insulator(FI) bilayer system, which is an important platform of spintronics. We considered a general model Hamiltonian with both spin-conserving and non-spin-conserving processes, and formulated the spin current and the spin-current noise within the framework of Keldysh Green's function [4]. Using the second-order perturbation with respect to the NM-FI interface coupling, we derived expressions of them in terms of the propagators of electrons and magnons. The lower panel of Fig. 1 shows temperature dependence of the spin-current noise using parameters for a yttrium-iron-garnet-(YIG-)platinum interface. As indicated from the figure, temperature dependences of the spin-current noise contain useful information, which can distinguish the mechanism of the spin-current generation.

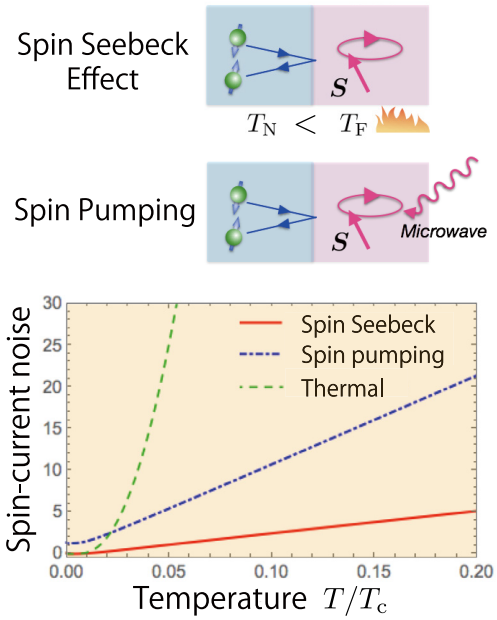

Fig. 1. Upper two pictures: Schematics of spin-current generation by spin Seebeck effect and spin pumping. Lower panel: Temperature dependence of spin-current noise. The temperature is normalized with the Curie temperature of the ferromagnetic insulator. Temperature dependence of thermal spin-current noise is also shown.

We also demonstrated that simultaneous measurement of the spin current and the non-equilibrium spin-current noise provides important information on spin transport. The Fano factor, which is the ratio between the spin-current noise and the spin current, was shown to be constant at low temperatures for both spin Seebeck effect and spin pumping. This low-temperature Fano factor includes information of effective spin in spin transport, which is $\hbar$ if the spin conserving process is dominant. As the weight of the spin non-conserving process increases, the effective spin increases by mixture of the two types of spin transport process. In actual experiments of spin pumping, the spin current can be generated also by spin Seebeck effect due to sample heating by microwave irradiation. Discrimination of spin pumping signal from heating effect has been a problem for long time. We proposed a method to estimate an increase of the sample temperature by combining the spin current and the spin-current noise. Finally, we discussed a spin Hall angle, which indicates an efficiency of the inverse spin Hall effect: conversion of spin current into charge current in metals. In a special situation, we can know the Fano factor a priori. For example, the Fano factor is $\hbar$ at low temperatures if the spin non-conserving process can be neglected. For such a situation, we can use it as a standard for the spin current and the spin current noise. By comparing this Fano factor with actual measurement of charge current and current noises in the inverse spin Hall effect, we can obtain the spin Hall angle at the interface.

We hope that the present calculation serves as a bridge between two well-established research areas, mesoscopic physics and spintronic physics. This collaborated research started from close discussion with M. Matsuo who was a visiting professor of ISSP in academic year 2016.

References
[1] A. Kamra *et al.*, Phys. Rev. B, **90**, 214419 (2014).
[2] A. Kamra and W. Belzig, Phys. Rev. Lett. **116**, 146601 (2016); S. Takei and M. Mohseni, Phys. Rev. B **97**, 014427 (2018).
[3] M. Matsuo, Y. Ohnuma, T. Kato, and S. Maekawa, Phys. Rev. Lett. **120**, 037201 (2018).
[4] Y. Ohnuma, M. Matsuo, and S. Maekawa, Phys. Rev. B **96**, 134412 (2017).

Authors
M. Matsuo[a,b], Y. Ohnuma[b], T. Kato, and S. Maekawa[b]
[a]Advanced Institute for Materials Research, Tohoku University
[b]Advanced Science Research Center, Japan Atomic Energy Agency

Spin-Orbit Interaction in Nanoparticle-Decorated Graphene

J. Haruyama and S. Katsumoto

Introduction of spin-orbit interactions (SOIs) into two-dimensional (2D) honeycomb lattices is predicted to create 2D topological phases [1]. Graphene is a representative 2D honeycomb lattice, whereas it lacks SOIs due to the

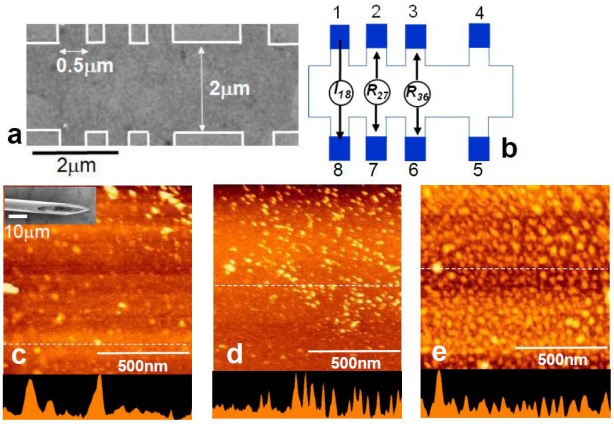

Fig. 1. (a)(b) Scanning electron micrograph and schematic top views of graphene formed into a multiple Hall bar pattern used for non-local resistance (R_{NL}) measurements. (c -e) Atomic force microscope images of the Bi_2Te_3 nanoparticle decorated on graphene using a nano needle method (inset of (c)) with three different-densities (D) ; (c) – (e) for D ~ 4/(100 nm)^2 (coverage ~ 3%), D ~ 10/(100 nm)^2 (coverage ~ 8%), and D ~ 23/(100 nm)^2 (coverage ~ 20%), respectively. Lower panels show the height along white broken lines in the upper panels.

lightness of carbon atom and the complete flatness of the lattice. Though many trials to introduce SOIs into graphene with various perturbations have been reported so far, the number of sound experiments has remained small [2]. A way to introduce SOI is to distribute nanoparticle with heavy mass atoms onto graphene. Here we precisely control small-amount of nanoparticles (platinum (Pt) or bismuth telluride (Bi_2Te_3)) randomly distributed on graphene and observe the appearance of SOI-induced (inverse) spin Hall effect (SHE).

Pt or Bi_2Te_3 nanoparticles with diameters of 3 ~ 5 nm are dispersed on monolayer graphene grown by chemical vapor deposition and formed into a multiple Hall bar (Figs. 1(a), 1(b); area for $w = 2 \times L_{sa} = 5(\mu m)^2$). High quality of the monolayer graphene has been confirmed by Raman spectra and X-ray Photoelectron Spectroscopy. The electron concentration in the graphene can be controlled with the back-gate voltage. For this experiment, we develop a specific tool, that is, a nano-needle to carry out clean and noninvasive decoration of graphene surface with nanoparticles. Dropping a small fleck of acetone, into which the nanoparticles are dispersed with ultrasound, we can precisely control the nanoparticle density (D) on the graphene surface. Examples of thus dispersed random nanoparticles are shown in Fig. 1 (c-e) for D ~ 4, 10 and 23/(100 nm^2), respectively. After the decoration, samples are annealed at 400 ºC for 10 minutes under high vacuum to advance chemical bonding between the nanoparticles and the carbons.

Figures 1 (b) also shows the terminal configuration for the non-local resistance measurement. The external current is applied along 1-8, which causes the spin current along the Hall bar via the SHE. The spin current next produces voltages between 2 and 7, 3 and 6 through the inverse SHE. Figure 2 shows the temperature variation of thus measured non-local resistance R_{27} as a function of in-plane external magnetic field, which causes the precession of electron spins and hence diminish the non-local resistance. This can be viewed as, in a sense, a Hanle measurement. The behavior of R_{27} shown in Fig. 2 clearly indicates the introduction of considerably strong SOI into graphene. The estimated spin separation by the SOI is as large as 50 meV, which is the largest among so far reported. The value is supported by scanning tunneling microscopy spectra.

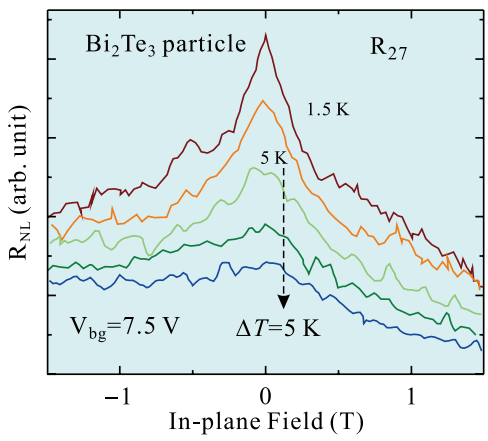

Fig. 2. Temperature variation of non-local resistance R_{27} as a function of in-plane external magnetic field.

References

[1] C. L. Kane and E. J. Mele, Phys. Rev. Lett. **95**, 226801 (2005).
[2] J. Balakrishnan, G. K. W. Koon, M. Jaiswal, A. C. Neto, and B. Özyilmaz, Nat. Phys. **9**, 284 (2013).

Authors

T. Namba[a], K. Tamura[a], K. Hatsuda[a], C. Ohata[a], T. Nakamura, S. Katsumoto, and J. Haruyama[a]
[a]Aoyama Gakuin University

STM Study of In-Gap Surface States on Single-Phase SmB_6 (001)

S. Suga, F. Iga, and F. Komori

Strong electron correlation in the Kondo insulator samarium hexaboride (SmB_6, Fig. 1(a)) has attracted great attention over decades. The hybridization of localized 4*f* states with itinerant 5*d* states triggers a gap opening at Fermi energy E_F, and induces a metal-insulator transition with decreasing temperature [1]. Recently, it was proposed that the observed saturation in the electrical resistivity at

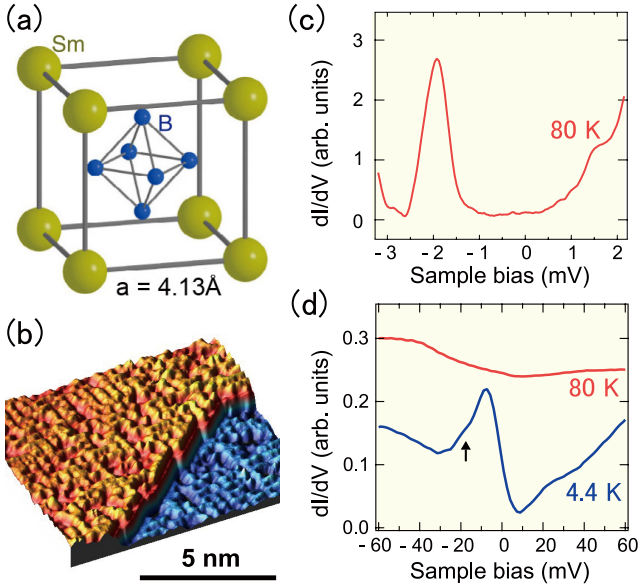

Fig. 1. (a) Schematic structure model of single-crystal SmB_6. (b) Atomically-resolved STM image of the SmB_6(001) surface prepared by the cycles of Ar^+ sputtering and 1030 ºC annealing. (c) Spatially-averaged *dI/dV* spectrum over a wide range of sample bias from -3.2 V to 2.2 V at 80 K. The peak at -2 V indicates Sm termination of the prepared SmB_6(001) surface. (d) Temperature dependence of the spatially-averaged *dI/dV* spectra on the SmB_6(001) surface in the hybridization gap area at 80 K and 4.4 K. The arrow indicates the fine shoulder structure located at -15 meV possibly derived from localized bulk f-states.

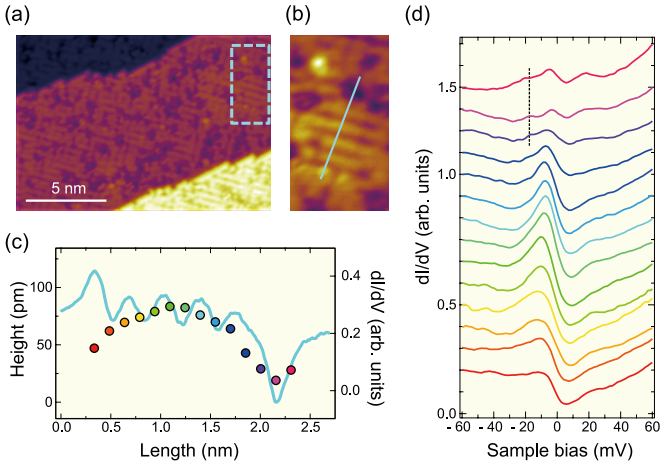

Fig. 2. (a) Atomically-resolved STM image of the $SmB_6(001)$ surface. (b) Magnified STM image of the $SmB_6(001)$ surface surrounded by blue dotted lines in (a). (c) (Left axis) STM height profile along the blue line in (b). Two types of defects, a small protrusion and a dip, are visible at ~ 0.3 (left) and at 2.2 (right) nm, respectively. (Right axis) differential conductivity *dI/dV* along the blue line in (b). At each position, the magnitude of the *dI/dV* of the peak structure located at -8 meV in (d) is plotted. (d) Series of 14 *dI/dV* spectra recorded along the blue line in (b). The colors indicate the recorded positions of the *dI/dV* spectra marked as dots with the same colors in (c), i.e, the spectra from bottom to top in (d) corresponds to the dots from left to right in (c). The dotted line indicates the energy position of a fine structure in the in-gap state.

low temperature is attributed to a topological surface state inside the hybridization gap. Experimentally, however, spatially-resolved surface characterizations by scanning tunneling microscopy (STM) have revealed that several types of surface structures randomly coexist on the cleaved $SmB_6(001)$ surfaces. This makes it difficult to investigate the intrinsic surface electronic properties by spatially-averaged methods. As an alternative to the crystal cleavage, a cyclic Ar^+ ion sputtering and annealing was recently performed to prepare a single-phase $SmB_6(001)$ surface reproducibly [2]. Nevertheless, the atomically-resolved structure characterization of the surface is still necessary for detailed discussion of its in-gap surface state.

Using STM, we have investigated structural and electronic properties of a clean $SmB_6(001)$ surface prepared by the sputtering and annealing method [3]. Our atomically-resolved observations shown in Fig. 1 (b) reveals that a non-reconstructed $p(1 \times 1)$ lattice with point defects is successfully and homogeneously formed over the entire surface using an optimal annealing temperature. In the tunneling (*dI/dV*) spectra on this surface, we found a peak in the density of states at – 2 eV below E_F (Fig. 1(c)), which indicates the B 2*p* dangling bonds on a Sm-terminated surface. The hybridization gap with an in-gap state located around – 8 meV below E_F develops in the tunneling spectra with decreasing temperature as shown in Fig. 1(d). In Fig. 2, we show spatial dependence of the in-gap state near E_F at 4.4 K. The state is sensitive to the structural variation on the surface; it is significantly suppressed near the point defect on the ordered region, but survives on the whole surface irrespective of defects. The existence of a robust surface state, which can be an evidence of a topologically-protected surface state, is confirmed inside the Kondo hybridization gap in this system.

References
[1] P. Coleman, Handbook of Magnetism and Advanced Magnetic Materials, **1**, 95 (Wiley, 2007).
[2] M. Ellguth, C. Tusche , F. Iga, and S. Suga, Philos. Mag. **96**, 3284, (2016).
[3] T. Miyamachi *et al.*, Sci. Rep. **7** 12837, (2017).

Authors
T. Miyamachi, S. Suga[a,b], M. Ellguth[c], C. Tusche[b,d], C. M. Schneider[b,d], F. Iga[e], and F. Komori
[a]Institute of Scientific and Industrial Research, Osaka University
[b]Peter Grünberg Institut, Forschungszentrum Jülich
[c]Institut für Physik, Johannes-Gutenberg-University
[d]Fakultät für Physik, Universität Duisburg-Essen
[e]Ibaraki University

Atomic Contacts Easily Broken by Bias Voltage under Tensile Stress

S. Kurokawa, Y. Hasegawa, and A. Sakai

A single-atom contact (SAC) of a metal is the smallest contact where a single atom makes a link between a pair of electrodes. One notable characteristic of SACs is found in their conductance, which is described as $(\Sigma_n \tau_n)G_0$. Here τ_n is the transmission probability of the n-*th* conduction channel and $G_0 = 2e^2/h$ is the quantum conductance. Among various metals, SACs of noble metals (Au, Ag, and Cu) are of particular physical and practical importance, because they have only a single conduction channel with $\tau_1 \sim 1$, making the conductance ~G_0; a material-independent constant. These unique characteristic makes them useful in logic circuits, and some atomic devices employing SACs as functional elements have already been developed.

For the device applications, SACs have to be stable under operating bias voltages. Conventionally, the stability of SACs is discussed in terms of their lifetime τ, which is given by the following thermal-activation-type-formula: $\tau = \tau_0 e^{W/kT}$; $W = W_0 - \alpha V - \beta F$ (α, $\beta > 0$), where τ_0 is a pre-exponential factor, V and F represent the bias and the tensile force applied to an SAC, respectively, and W_0 is the activation barrier at $V = F = 0$. The term αV represents the reduction of the barrier by the bias voltage. Similarly, the term βF determines the ultimate tensile strength to break the SAC.

In the equation, both V and F additively contribute to reduce the activation barrier and shorten the lifetime, which means that the bias stability depends on the amount of F. To date, the bias stability has been experimentally studied for some metal SACs that had been, in most cases, prepared by mechanical breaking, which is usually subjected to

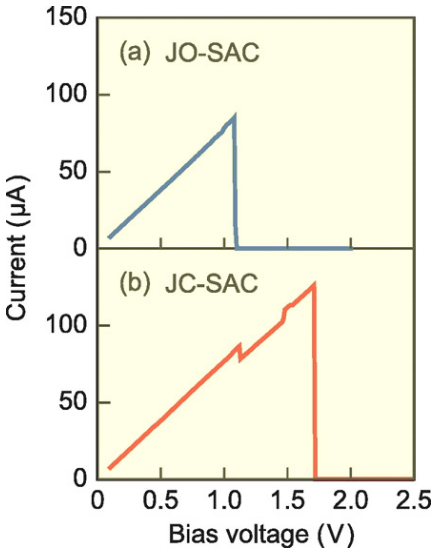

Fig. 1. Examples of I–V curves observed at Au SACs produced (a) by junction opening (JO) and (b) by junction closing (JC). The junction current increases linearly up to the high-bias breakdown.

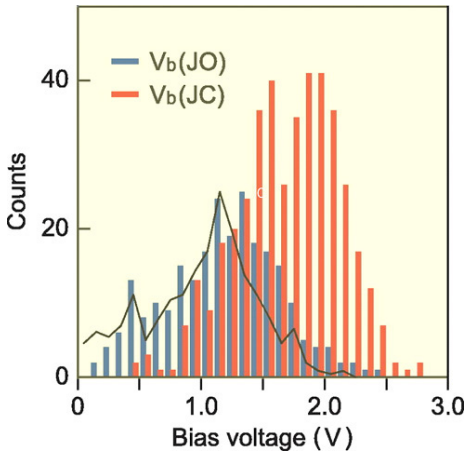

Fig. 2. The distribution of the junction breaking voltages of Au SACs. The blue and red histograms represent the distributions for JO- and JC-SACs, respectively. The solid line indicates the V_b data for JO-SACs collected by Smit *et al*. [3] The distribution of JC (red) is obviously shifted to the high bias side compared to that of JO (blue). The observed high-bias shift of V_b for JC indicates high stability of JC-SACs against the bias voltage applied across the junction.

built-in tensile stress. In this work [1], we investigated the break voltages of Au and Pb SACs created by junction closing (JC), instead of breaking, and compared the results with those produced by junction opening (JO) or breaking. Because JC essentially involves no junction stretching, the JC-SACs should contain lower tensile forces than JO-SACs and are thus expected to show higher break voltages.

Our break-voltage measurements were made on Au contacts produced by mechanically controllable break junction (MCBJ) method at 4 K. We also performed similar break-voltage experiments on Pb SACs using a cryogenic ultrahigh-vacuum STM at 1.7 K and fabricated Pb SACs by touching a Pb-coated tungsten tip to a clean Pb surface [2].

Figures 1(a) and 1(b) show examples of the I–V curves observed for JO- and JC-SACs, respectively. In both I–V curves, the junction current increases with the voltage and suddenly drops to zero at the point of break junction. From the breaking point we determined the break voltage V_b. Figure 2 summarizes the results of our V_b measurements on Au SACs. In the figure, the two histograms colored in blue and red represent the distributions of V_b for JO- and JC-SACs, respectively. Both histograms cover a wide voltage range, but the distribution of JC (red) is obviously shifted to the high bias side compared to that of JO (blue). The observed high-bias shift of V_b for JC confirms our assumption that JC-SACs show higher break voltages than JO-SACs.

We also measured the break voltages of Pb SACs. The V_b distribution of JC moves to the high bias side relative to that of JO. Thus, as for Au, the JC-SACs of Pb tend to break at higher biases than the JO-SACs. The observed high-bias shift of JC indicates that JC is a viable method for improving the bias stability of SACs.

From our results we also estimated the magnitude of the force reduction in our Au JC-SACs. According to the equation mentioned above, a variation in the tensile force ΔF is related to the variation in the break voltage ΔV_b as $\Delta F = -(\alpha/\beta)\Delta V_b$. Our ΔV_b for Au SACs is 0:52 V. Substituting the value of α and β adapted from Ref. 3, we obtain the force reduction ΔF = 0:15 nN. Smit et al. [3] estimated F in JO is 0.95 nN; thus, we find F in JC is 0.80 nN. This indicates that the JC reduced the tensile force as expected, but the force was still positive and remained tensile.

The tensile force in JC might appear counter-intuitive because a JC-SAC is formed by the touching of two electrodes. We consider that it is due to the short-range attractive force. At the close distances the apex atom moves towards the counter electrode by the attractive force exerted on the atom. As a result, the bonds between the contact atom and the electrode atoms are slightly stretched and exert a tensile force on the contact atom. This explains why we obtained tensile force for our Au JC-SACs.

Our break voltage measurements of Au and Pb SACs indicated that the JC-SACs exhibit a higher break voltage than the JO-SACs, which is favorable for the device application. The improved tolerance against the bias voltage can be understood by the reduced tensile stress in JC-SACs, clarifying the interplay between the junction force and the bias stability in SACs.

References
[1] S. Wakasugi, S. Kurokawa, H. Kim, Y. Hasegawa, and A. Sakai, J. Appl. Phys. **121**, 244304 (2017).
[2] H. Kim and Y. Hasegawa, Phys. Rev. Lett. **114**, 206801 (2015).
[3] R. H. M. Smit, C. Untiedt, and J. M. van Ruitenbeek, Nanotechnology **15**, S472 (2004).

Authors
S. Wakasugi[a], S. Kurokawa[a], H. Kim, Y. Hasegawa, and A. Sakai[a]
[a]Kyoto University

Noble Metal Segregation in $SrTiO_3$

M. Lee and M. Lippmaa

Photoelectrochemical water splitting is a process where photoexcited electrons and holes are used to drive a chemical hydrogen or oxygen evolution reaction at the surface of a semiconductor photoelectrode. The technique can be used to harvest solar energy and store the energy in the form of hydrogen fuel. In the semiconductor materials studied so far, the solar-to-hydrogen conversion process efficiency is still too low for practical applications. Oxide semiconductors such as titanates are often used as the electrode materials due to the chemical stability in water, but the energy conversion efficiency is limited by the loss of photocarriers to trapping and recombination. A general solution to this problem is to construct a nanostructured photoelectrode where light can be efficiently absorbed but a short escape path exists for the photocarriers to reach the surface before recombination can occur. For example, an array of semiconductor nanowires can be used, which would increase the effective surface area, guarantees a short carrier escape path in the radial direction of a wire, while still efficiently absorbing incident sunlight. A drawback of this strategy is the complicated synthesis

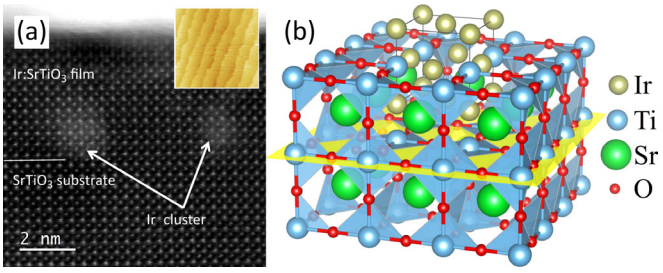

Fig. 1. (a) Cross-sectional HAADF-STEM image of a Ir:$SrTiO_3$ film on a $SrTiO_3$ substrate showing the formation of bright Ir clusters at the film interface. (inset) AFM image of the film surface, showing a smooth step-and-terrace morphology. (b) Structural model of a lattice-matched fcc Ir metal inclusion in the $SrTiO_3$ lattice.

process of nanowires and limited long-term mechanical stability. We have therefore studied the possibility of using spontaneous noble metal segregation in a perovskite lattice to embed self-organized nanoscale metal electrodes in the bulk of an oxide semiconductor. We have demonstrated the formation of Ir nanopillars in $SrTiO_3$ thin films and photoelectrochemical measurements have shown that embedding metal electrodes in a semiconductor does indeed improve the energy conversion efficiency [1]. The main benefit of this structure is the simple one-step synthesis process and mechanical robustness.

The purpose of this joint-use project was to study the initial stage of Ir metal segregation in $SrTiO_3$ thin films [2]. As shown in the inset of Fig. 1a, the surface morphology of thin Ir:$SrTiO_3$ (~5 unit cell) films imaged by atomic force microscopy (AFM) shows no obvious metal segregation effects. However, bright clusters are observed in high-angle annular dark field scanning transmission electron microscopy (HAADF-STEM) images. An in-situ energy-dispersive x-ray spectroscopic analysis showed that the bright clusters in the film are strongly enriched in Ir and consistent with a face-centered cubic (fcc) metal cluster embedded in the perovskite lattice, as illustrated in Fig. 1b. It is clear from the STEM analysis that the clusters have uniform lateral size of about 2 × 2 perovskite unit cells. The thin films were grown at strongly reducing conditions, which means that the perovskite lattice contains oxygen vacancies, promoting the substitution of Ir atoms at the anion site. The anion substitution allows the fcc metal to form a lattice-matched metal inclusion in the $SrTiO_3$ lattice. When similar films are grown at slightly more oxidizing conditions, extended Ir metal nanopillars form instead of the isolated metal clusters. This work helps to design more elaborate oxide metal nanocomposites for energy harvesting applications.

References

[1] S. Kawasaki, R. Takahashi, T. Yamamoto, M. Kobayashi, H. Kumigashira, J. Yoshinobu, F. Komori, A. Kudo, and M. Lippmaa, Nat. Commun. **7**, 11818 (2016).

[2] M. Lee, R. Arras, R. Takahashi, B. Warot-Fonrose, H. Daimon, M.-J. Casanove, and M. Lippmaa, ACS Omega **3**, 2169 (2018).

Authors

M. Lee[a], R. Arras[b], R. Takahashi, B. Warot-Fonrose[b], H. Daimon[a], M.-J. Casanove[b], and M. Lippmaa

[a]Nara Institute of Science and Technology

[b]Université de Toulouse

Discovery of 'Quantum' Supercritical State of an Electron Fluid Induced by Valence Fluctuations

S. Nakatsuji, S. Shin, and T. Sakakibara

The supercritical fluid state near the liquid-gas critical point has been a major subject in condensed matter physics for its technological relevance and for its scientific significance. One of the important goals is to bring down the critical temperature and pressure, which are normally much higher than ambient conditions. By contrast, in the electronic versions of these critical points, there are some cases where the temperature scale may be reduced significantly down to near-zero temperatures so that one may observe quantum critical phenomena in the corresponding "supercritical" states. Strange metal behaviors have been seen in correlated electron systems as a result of proximity

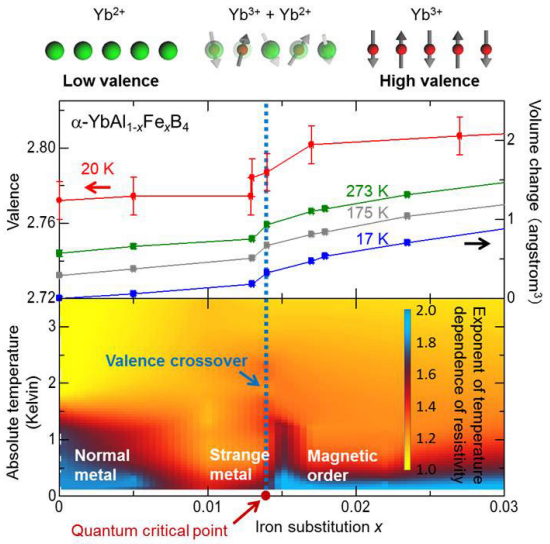

Fig. 1. Emergent quantum valence supercritical state in α-$YbAl_{1-x}Fe_xB_4$ at x = 0.014 exhibiting the sharp change in the valence, volume and the power law exponent in the temperature dependence of the resistivity. The high valence state and the low valence state are fluctuating around the valence crossover region as illustrated at the top of the figure. Here the arrows indicate the magnetic moments of the Yb^{3+} ion (red sphere). The middle of the figure shows the sharp valence change at around x = 0.014 at the absolute temperature of 20 Kelvin determined by the hard x-ray photoelectron spectroscopy (HAXPES). Significantly, the volume shows a similar x dependence to the valence. The contour plot at the bottom of the figure highlights the strange metallic state (yellow highlighted regions) emergent concomitantly with the sharp valence crossover at x = 0.014 between the normal metallic and magnetic ordered states. The contour plot indicates the variation of the power law exponent of the temperature dependence of the resistivity. The valence quantum critical point exists at x = 0.014 and at absolute zero temperature.

to a quantum critical end point of a first-order transition such as a metamagnetic transition and a Mott transition. Another candidate for the density instability that may theoretically drive novel quantum criticality (QC) is valence transition [1]. Near its associated quantum critical end point, singular fluctuations of valence (which includes charge, spin, and orbital degrees of freedom) and its coupling with thermodynamic quantities are expected to lead to a strong violation of Fermi liquid (FL) behavior. Similar to the Widom line in the supercritical fluid [2], fluctuations remain strong near the valence crossover line. Although a valence crossover at low temperatures has been reported in a variety of materials [3, 4], the associated QC has not been confirmed to date.

A valence critical end point existing near the absolute zero provides a unique case for the study of a quantum version of the strong density fluctuation at the Widom line in the supercritical fluids. Although singular charge and orbital dynamics are suggested theoretically to alter the electronic structure significantly, breaking down the standard quasiparticle picture, this has never been confirmed experimentally to date. We provide the first empirical evidence that the proximity to quantum valence criticality leads to a clear breakdown of Fermi liquid behavior. Our detailed study of the mixed valence compound α-$YbAlB_4$ reveals that a small chemical substitution induces a sharp valence crossover, accompanied by a pronounced non–Fermi liquid behavior characterized by a divergent effective mass (Fig. 1) and unusual T/B scaling in the magnetization.

References

[1] S. Watanabe and K. Miyake, Phys. Rev. Lett. **105**, 186403 (2010).

[2] B. Widom, J. Chem. Phys. **43**, 3898 (1965).

[3] J.-P. Rueff *et al.*, Phys. Rev. Lett. **106**, 186405 (2011).

[4] K. Matsubayashi *et al.*, Phys. Rev. Lett. **114**, 086401 (2015).

Authors
K. Kuga[a], Y. Matsumoto, M. Okawa, S. Suzuki, T. Tomita, K. Sone, Y. Shimura, T. Sakakibara, D. Nishio-Hamane, Y. Karaki[b], Y. Takata[a], M. Matsunami[c], R. Eguchi[d], M. Taguchi[a], A. Chainani[a,e], S. Shin[a], K. Tamasaku[a,f], Y. Nishino, M. Yabashi, T. Ishikawa, S. Nakatsuji[g]
[a]RIKEN SPring-8 Center
[b]University of the Ryukyus
[c]Institute for Molecular Science and The Graduate University for Advanced Studies
[d]Okayama University
[e]National Synchrotron Radiation Research Center
[f]Hokkaido University
[g]Japan Science and Technology Agency

Discovery of a New Magnetic Material: "Weyl Magnet"

S. Nakatsuji, T. Kondo, and S. Shin

In 2015, Weyl fermions have been discovered for the first time near the Fermi level in the non-magnetic semimetal TaAs. Weyl points in the momentum space serve as a pair of magnetic monopoles through the topological aspects of the wavefunctions for electrons [1]. Moreover, the fictitious magnetic fields due to the monopoles may induce novel electric transports, and could be useful for low energy consumption electronics. In contrast to the non-magnetic Weyl fermions in TaAs, magnetic Weyl fermions are known to appear in magnets, thus would enable us to control Weyl fermions by external magnetic field. This functionality will be necessary for device applications, and many efforts have been made for searching magnetic Weyl fermions. However, they have remained hypothetical so far.

Recently, an antiferromagnetic manganese-tin alloy Mn_3Sn is found to exhibit a large anomalous Hall and Nernst effects, even at room temperature [2, 3]. Usually, these anomalous Hall and Nernst effects are known to be proportional to magnetization and thus have been observed only in ferromagnets. The spontaneous Hall resistivity in the antiferromagnet with vanishingly small magnetization indicates that the large fictitious field equivalent to a few hundred T must exist in the momentum space. Recent DFT calculation predicts that the large fictitious field or Berry curvature may well appear due to the formation of Weyl points nearby the Fermi energy E_F [4].

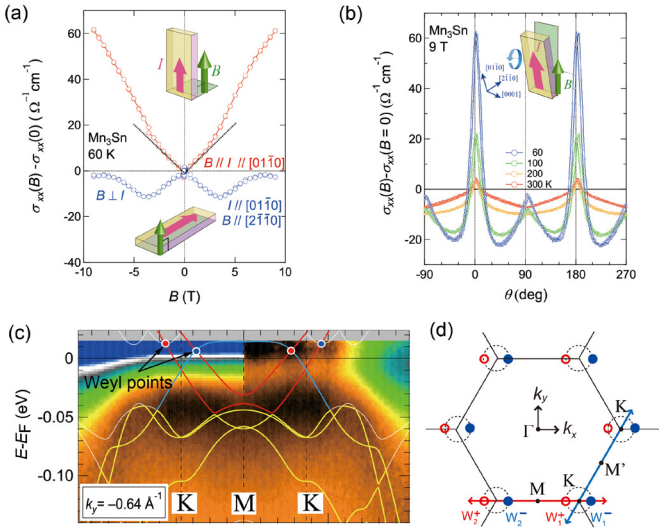

Fig. 1. Evidence for Weyl fermions in Mn_3Sn:(a)Weyl fermions in condensed matter systems show an unconventional positive longitudinal magnetoconductivity (negative longitudinal magnetoresistivity), called "chiral anomaly". (b) This appears only when magnetic field is applied parallel to electric field ($B//I$, θ = 0 deg.). With an increasing magnetic field, the breaking of the imbalanced charge conservation between the Weyl points with opposite chirality makes the materials more conductive. This novel phenomenon is known as one of the experimental evidence of the Weyl fermions. (c) ARPES band mapping near the Fermi level is compared with DFT band calculations. Weyl (band crossing) points with opposite chirality are denoted by blue and red closed circles, respectively. (d) These Weyl points are found along the K–M–K line in the bands on the $k_z = 0$ plane near E_F.

Nakatsuji, Kondo and Shin groups at ISSP University of Tokyo and their theoretical collaborators at RIKEN have demonstrated the realization of magnetic Weyl fermions in Mn_3Sn for the first time. Our study has revealed the existence of a "Weyl magnet", a new magnet with tunable magnetic Weyl fermions by magnetic fields at room temperature [5]. We found strong experimental evidence for the Weyl fermions in Mn_3Sn, namely, that the band structure revealed by angle resolved photoemission spectroscopy (ARPES) is found roughly consistent with density functional theory (DFT) and the chiral anomaly is clarified in the magnetotransport measurements (Fig. 1). Thus, these experiments demonstrate that the large anomalous Nernst signals arise from the Berry curvature associated with the Weyl points near the Fermi energy.

Our groups have revealed extremely large magnetic transports and thermoelectric effects in the Mn_3Sn magnet. By their new discovery of Weyl magnet, the mystery of these novel properties would be solved. We anticipate that further new phenomena will emerge through the interplay between electron correlation and topology in Weyl magnets.

References
[1] B. Q. Lv, H. M. Weng, B. B. Fu, X. P. Wang, H. Miao, J. Ma, P. Richard, X. C. Huang, L. X. Zhao, G. F. Chen, Z. Fang, X. Dai, T. Qian, and H. Ding, Phys. Rev. X **5**, 031013 (2015).
[2] S. Nakatsuji, N. Kiyohara, and T. Higo, Nature **527**, 212 (2015).
[3] M. Ikhlas, T. Tomita, T. Koretsune, M. –T. Suzuki, D. Nishio-Hamane, R. Arita, Y. Otani, and S. Nakatsuji. Nature Physics **13**, 1085 (2017).
[4] H. Yang, Y. Sun, Y. Zhang, W-J. Shi, S. S. P. Parkin, and B. Yan, New J. Phys. **19**, 015008 (2017).
[5] K. Kuroda, T. Tomita, M.-T. Suzuki, M.-T. Suzuki, C. Bareille, A. A. Nugroho, P. Goswami, M. Ochi, M. Ikhlas, M. Nakayama, S. Akebi, R. Noguchi, R. Ishii, N. Inami, K. Ono, K. Kumigashira, A. Varykhalov, T. Muro, T. Koretsune, R. Arita, S. Shin, T. Kondo, and S. Nakatsuji, Nature Materials **16**, 1090 (2017).

Authors
K. Kuroda*, T. Tomita*, M.-T. Suzuki[a], C. Bareille, A. A. Nugroho[b], P. Goswami[c], M. Ochi[d], M. Ikhlas, M. Nakayama, S. Akebi, R. Noguchi, R. Ishii, N. Inami[e], K. Ono[e], K. Kumigashira[e], A. Varykhalov[f], T. Muro[g], T. Koretsune[a], R. Arita[a], S. Shin, T. Kondo, and S. Nakatsuji
[*equal contribution]
[a]RIKEN Center for Emergent Matter Science
[b]Institut Teknologi Bandung
[c]University of Maryland
[d]Osaka University
[e]High Energy Accelerator Research Organization (KEK)
[f]Elektronenspeicherring BESSY II
[g]Japan Synchrotron Radiation Research Institute (JASRI)

First-order Magnetic Transitions and Transformation Arrested Behaviors in Sn-Modified Mn_2Sb

Y. Mitsui, K. Koyama, and Y. Uwatoko

First-order magnetic transition (FOMT) has been paid much attention such as the large magnetocaloric effects and metamagnetic shape memory effects. FOMT in some magnetic functional materials suppressed under high

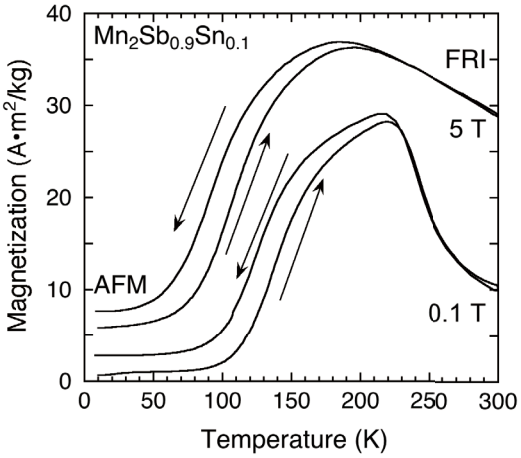

Fig. 1. Thermomagnetization curves for $Mn_2Sb_{0.9}Sn_{0.1}$ under 0.1 and 5 T [4].

magnetic fields. The suppression of FOMT is due to the freezing of the phase transition, which is explained by glass-like dynamics. This phenomenon is called "kinetic arrest" or "thermal transformation arrest (TTA)". For the application of magnetic functional materials using FOMT, the investigation of the origin of TTA phenomenon is necessary.

Mn_2Sb-based compounds exhibit FOMT between ferrimagnetic (FRI) and antiferromagnetic (AFM) state. So far, magnetocaloric effects for Mn_2Sb-based system were examined [1]. Although Mn_2Sb is ferrimagnet and do not show FOMT, FRI-AFM transition exhibits by substitution of V, Cr, Co and Cu to Mn-site. Additionally, it is reported that Co-, and Cu-modified Mn_2Sb exhibited TTA phenomenon [2, 3]. Meanwhile, modification of Sb-site, such as $Mn_2Sb_{1-x}Ge_x$ [3] and $Mn_2Sb_{1-x}Sn_x$, also exhibits FRI-AFM transition. However, there are few reports about TTA phenomenon for these compounds. In this paper, we reported the thermal transformation arrest behavior of Sn-modified Mn_2Sb by magnetization measurements [4].

Figure 1 shows the thermomagnetization (M-T) curves in $Mn_2Sb_{0.9}Sn_{0.1}$ under μ_0H = 0.1 and 5 T. FRI-AFM phase transition were observed for 100 ≤ T ≤ 210 K at μ_0H = 0.1 T. It is found that the temperature region of FOMT in $Mn_2Sb_{0.9}Sn_{0.1}$ is wider than other Mn_2Sb-based systems, such as $Mn_{1.8}Co_{0.2}Sb$ [2] and $Mn_2Sb_{0.9}Ge_{0.1}$ [3]. On the other hand, the difference in M between heating process after zero-field cooling and in-field cooling were observed for T < 50 K in 5 T. It is suggested that the FRI-AFM transition were suppressed and residual FRI state existed. In other words, FRI state was arrested at in-field cooling process under 5 T.

For further investigation for the difference of magnetization, magnetic relaxation measurements were carried out. Figure 2 shows the magnetic relaxation curves at 10, 30 and 50 K under 5 T. The measurements were performed after in-field cooling under 5 T. Although the fraction of arrested FRI state was small, magnetization clearly decreased both 30 and 50 K with increasing time, indicating the relaxation from arrested-FRI state to AFM state.

In conclusion, magnetic properties of Sn-modified Mn_2Sb were investigated. It is suggested by magnetic relaxation measurements that TTA phenomenon exhibits in $Mn_2Sb_{0.9}Sn_{0.1}$.

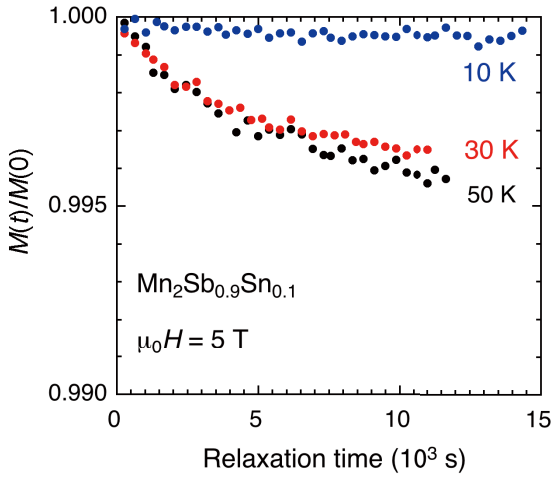

Fig. 2. Magnetic relaxation curves for $Mn_2Sb_{0.9}Sn_{0.1}$ at 10, 30, and 50 K in 5 T [4]. The magnetization $M(t)$ was normalized by $M(0)$.

References

[1] L. Caron *et al.*, Appl. Phys. Lett. **103**, 112404 (2013).
[2] H. Orihashi *et al.*, Mater. Trans. **54**, 969 (2013).
[3] Y. Matsumoto *et al.*, IEEE Trans. Magn. **50**, 1000704 (2014).
[4] T. Wakamori *et al.*, AIP Conf. Proc. **1763**, 020006 (2016).
[5] T. Wakamori *et al.*, IEEE Magn. Lett. **8**, 1402404 (2017).

Authors

Y. Mitsui[a], T. Wakamori[a], K. Takahashi[b], R. Y. Umetsu[b], Y. Uwatoko, M. Hiroi[a], K. Koyama[a],
[a]Kagoshima University
[b]Institute for Materials Research, Tohoku University

High Pressure Electrical Resistivity Measurements for High-T_c Candidates Material $Ln_4Ni_3O_8$ (Ln=La, Nd, Sm)

M. Uehara, I. Umehara, and Y. Uwatoko

$Ln_4Ni_3O_8$ (Ln=La, Nd, Sm) contains NiO_2 planes and its crystal structure is basically the same with high-T_c cuprate, and the formal valence of Ni is +1.33 composed of $3d^9$ and $3d^8$ mixed-valence state, being the same with high-T_c cuprate. Therefore, this compound seems to be a promising candidate for new high-T_c material. Despite these similarities with cuprate, this compound had showed neither metallic characteristic nor superconductivity [1-3], until we found that the intercalation and subsequent deintercalation treatment with sulfur (S-treatment) induced the metallic nature down to ~20 K (below ~20 K resistivity shows semiconducting upturn) in $Nd_{3.5}Sm_{0.5}Ni_3O_8$ [4, 5]. The sample without S-treatment is named to be the "as-synthesized sample" and the sample after S-treatment to be the "S-deintercalated samples" in this report. The as-synthesized and S-deintercalated samples are semiconducting and metallic (above ~20 K), respectively.

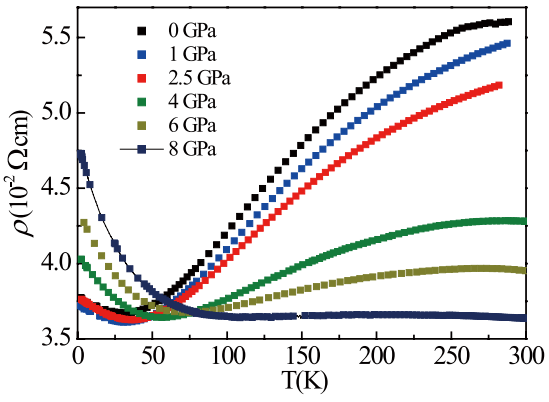

Fig. 1. Temperature dependence of electrical resistivity for the S-deintercalated sample of $Nd_{3.5}Sm_{0.5}Ni_3O_8$ under pressure.

Rietveld analyses based on synchrotron X-ray diffraction data at room temperature obtained in KEK suggest the removal of excess oxygens at apical site of Ni(2) which is in the outermost NiO_2 plane by S-treatment [6]. Therefore, it can be inferred that the excess oxygens at apical site of Ni(2) impedes the metallic conduction and these are effectively removed by the S-treatment. The similar situation has been discussed on the role of reduction annealing necessary procedure to obtain superconductivity for T'-type high-T_c cuprate having a very similar structure to present system.

In order to see whether or not the semiconducting behavior at low-temperature is suppressed and the superconductivity emerges, electrical resistivity measurements at pressures up to 8 GPa were performed for metallic S-deintercalated sample, and the cubic anvil apparatus was used with a mixture of Fluorinert 70 and 77 as the pressure medium. The result is shown in Fig. 1. In the temperature range from 300 K to approximately 50–60 K, the electrical resistivity is decreased by applying pressure. However, below approximately 50–60 K, with increasing applied pressure, the electrical resistivity increases and the temperature where the electrical resistivity shows an upturn from metallic conductivity increases, displaying enhancement of the semiconducting nature. As the origin of this unexpected result it can be speculated as follows: the removal of excess apical oxygens by S-deintercalation is not perfect. The pressure pushes the remnant apical oxygens close to the NiO_2 plane, and the effect of random potential increases, enhancing the tendency of localization. Similar pressure effect has been observed in T'-type high-T_c cuprate.

In conclusion, S-treatment removes additional apical oxygen but the removal is not perfect under the present S-treatment condition. Therefore, superconductivity might appear when additional apical oxygen is completely removed out.

References

[1] V. V. Poltavets *et al.*, Phys. Rev. Lett. **104**, 206403 (2010).
[2] Y. Sakurai *et al.*, Physica C. **487**, 27 (2013).
[3] Y. Sakurai *et al.*, JPS Conf. Proc. **1**, 012086 (2014).
[4] A. Nakata *et al.*, Adv. Condens. Matter Phys. **2016**, 5808029 (2016).
[5] K. Kobayashi *et al.*, JJAP Conf. Proc. **6**, 011106 (2017).
[6] M. Uehara *et al.*, J. Phys. Soc. Jpn. **86**, 114605 (2017)

Authors

M. Uehara[a], K. Kobayashi[a], H. Yamamoto[a], K. Wakiya[a] and I. Umehara[a], J. Gouchi, and Y. Uwatoko

[a]Yokohama National University

Maximizing T_c by Tuning Nematicity and Magnetism in $FeSe_{1-x}S_x$ Superconductors

K. Matsuura, Y. Uwatoko, and T. Shibauchi

In iron pnictides, high-T_c superconductivity appears near the antiferromagnetic phase, which is accompanied by the tetragonal-to-orthorhombic structural transition with significant electronic anisotropy (nematicity). It has been discussed that the quantum fluctuations of nematic and/or antiferromagnetic orders may play an essential role for the superconductivity. However, these two orders coexist with each other in iron-pnictide superconductors, and thus it has been difficult to disentangle the role of each phase for the superconductivity. To address this issue, FeSe is an important material because it shows a non-magnetic nematic order below 90 K [1]. Moreover, by isovalent S-substitution which corresponds to the chemical pressurization, this order is suppressed with increasing the S-content and it has been found that a non-magnetic nematic quantum critical point exists in the phase diagram of $FeSe_{1-x}S_x$ [2]. On the other hand, the non-magnetic nematic phase is also suppressed under physical pressure in FeSe, but before reaching a quantum critical point, a dome-shaped magnetic order is induced, which competes with high-T_c superconducting phase [3].

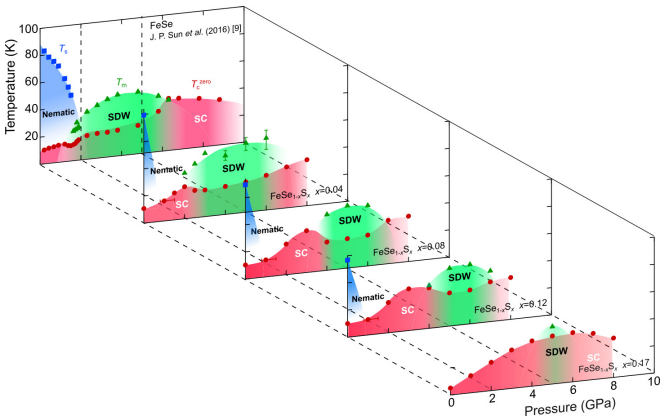

Fig. 1. Temperature-pressure-concentration phase diagram in $FeSe_{1-x}S_x$. The structural (T_s, blue squares), magnetic (T_m, green triangles) and superconducting transition temperatures (T_c^{zero}, red circles) are plotted against hydrostatic pressure P and S content x. T_s, T_m and T_c^{zero} are defined respectively by the temperatures of upturn, kink and zero resistivity in $\rho(T)$ curves under pressure for x = 0.04, 0.08, 0.12 and 0.17.

Here we report on our high pressure study on $FeSe_{1-x}S_x$ in wide ranges of pressure (up to $P \sim 8$ GPa) and sulfur content ($0 < x \leq 0.17$) by the electronic resistivity measurements with a cubic anvil high pressure apparatus in Uwatoko group and X-ray diffraction measurements with a diamond anvil cell in SPring-8 [4].

Our single crystalline samples were synthesized by the chemical vapor transport method. The electric resistivity measurements were carried out for $FeSe_{1-x}S_x$ (x = 0.04, 0.08, 0.12, and 0.17). From the anomalies seen in the temperature dependence of the electrical resistivity, the tetragonal-to-orthorhombic structural transition temperature T_s corresponding to the electronic nematic transition, the superconducting transition temperature T_c and the magnetic phase transition temperature T_m are determined, and their pressure dependence is investigated. From the results, we establish a three-dimensional Temperature(T)-pressure(P)-S substitution(x) electronic phase diagram as shown in Fig. 1. As x increases, the pressure-induced magnetic dome shifts to higher pressure and shrinks, while the low-pressure non-magnetic nematic phase shifts to lower pressure and disappears at $x \sim 0.17$. From this change, we find that the non-magnetic nematic and magnetic phases are completely separated in a low pressure region. To confirm the separation between two phases under pressure, we performed synchrotron X-ray diffraction under pressure for x = 0.08. In Fig. 2 we show (331) Bragg intensity as a function of temperature at 3.0 and 4.9 GPa together with the ρ(T) and dρ/dT data. At 3.0 GPa, no discernible change of the Bragg-peak is observed down to 10 K. At 4.9 GPa, on the other hand, the splitting of the Bragg peak is resolved around $T_s \sim 41$ K, evidencing the presence of the tetragonal-orthorhombic structural transition. This structural transition is located very close to the magnetic transition at T_m at 5.0 GPa as indicated by the sharp peak in dρ/dT curve. Thus, it

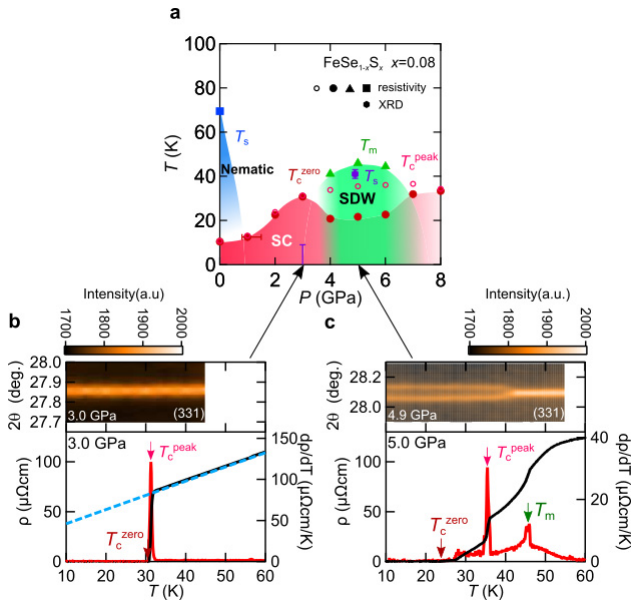

Fig. 2. (a) Temperature-pressure phase diagram for $FeSe_{1-x}S_x$ (x = 0.08) together with T_s determined by the high-pressure synchrotron X-ray diffraction (XRD) in a diamond anvil cell (the purple hexagon with error bars). (b), (c) Temperature dependence of Bragg intensity as a function of 2θ angle is indicated in color scale for 3.0 GPa (b) and 4.9 GPa (c). $\rho(T)$ and $d\rho/dT$ are also shown with the same horizontal axis. The red, pink and green arrows indicate T_c^{zero}, T_c^{peak} and T_m, respectively.

is natural to consider that the magnetic phase is accompanied with an orthorhombic structure, similar to the case of the stripe-type magnetic phase in other iron-pnictide superconductors.

By simultaneously tuning chemical and physical pressures, we achieve a complete separation of nematic and antiferromagnetic phases. In between, an extended non-magnetic tetragonal phase emerges, where T_c shows a striking enhancement. The high T_c superconductivity is observed near both ends of the magnetic dome. From this result, the fluctuations of magnetic order are likely to be more relevant to the high-T_c superconductivity in this system.

References

[1] S-H. Baek *et al*., Nature Materials **14**, 210 (2015).
[2] S. Hosoi *et al*., Proc. Natl. Acad. Sci. USA **113**, 8139 (2016).
[3] J. P. Sun *et al*., Nat. Commun. **7**, 12146 (2016).
[4] K. Matsuura *et al*., Nat. Commun. **8**, 1143 (2017).

Authors

K. Matsuura[a], Y. Mizukami[a], Y. Arai[a], Y. Sugimura[a], N. Maejima[b], A. Machida[b], T. Watanuki[b], T. Fukuda[c], T. Yajima, Z. Hiroi, K. Y. Yip[d], Y. C. Chan[d], Q. Niu[d], S. Hosoi[a], K. Ishida[a], K. Mukasa[a], S. Kasahara[e], J.-G. Cheng[f], S. K. Goh[d], Y. Matsuda[e], Y. Uwatoko, and T. Shibauchi[a]
[a]University of Tokyo
[b]National Institutes for Quantum and Radiological Science and Technology
[c]Japan Atomic Energy Agency (SPring-8/JAEA)
[d]The Chinese University of Hong Kong
[e]Kyoto University
[f]Chinese Academy of Sciences

Torque Magnetometry Studies using the Microcantilever on Molecular Conductor TPP[Mn(Pc)(CN)$_2$]$_2$

K. Torizuka, M. Matsuda, and Y. Uwatoko

The shape of the Metal Phthalocyanine TPP[M(Pc)(CN)$_2$]$_2$ compound (M = 3d metal) is unique; two CN groups are perpendicularly attached to the center of the M(Pc) planar molecule. In these compounds, the magnetic d electron of the central ion in the planar molecule and the conducting π electron reside in the same unit molecule. This fact makes the interaction between d and π electrons important. In M = Fe, the compound exhibits a giant negative magnetoresistance (GMR); when a high magnetic field is applied perpendicularly to the c-axis, the resistivity drops by more than two orders of magnitude at low temperatures. On the other hand, M = Mn, GMR is hardly seen. The motivation of our research is to know the difference in magnetic structure between compounds that GMR can be seen and compounds that GMR cannot be seen.

Here we report the results of our torque magnetometry experiments on M = Mn compound, TPP[Mn(Pc)(CN)$_2$]$_2$, using the microcantilever for the atomic force microscopy (AFM). This technique is very powerful, because even if the sample mass is on the order of 1 μg, it is so sensitive that we can detect the torque signal. In our experiments only tiny sample is available. The sample was mounted at the tip of the cantilever and the magnetic field orientation dependence of the signal that is nonlinearly proportional to the torque was measured.

In Figs. 1 and 2, typical torque curves measured when the magnetic field was rotated in the plane that includes the c-axis, and when the magnetic field was rotated in the ab plane, are depicted, respectively. A twofold symmetric signature with large and small peaks is seen in Fig. 1, which has never been observed in our former measurements on TPP[Fe(Pc)L$_2$]$_2$ (L = CN, Br, and Cl) family. This is characteristic of the ferromagnetism. On the other hand, a sawtooth waveform and fourfold-symmetric behavior can be seen

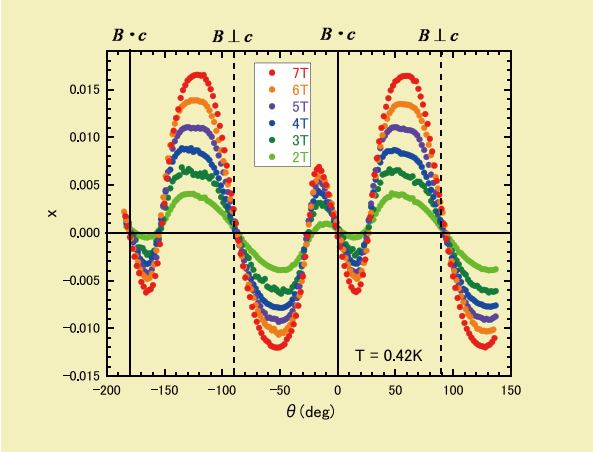

Fig. 1. Torque curves under various magnetic fields when the magnetic field was rotated in a plane included the c-axis at 0.42 K.

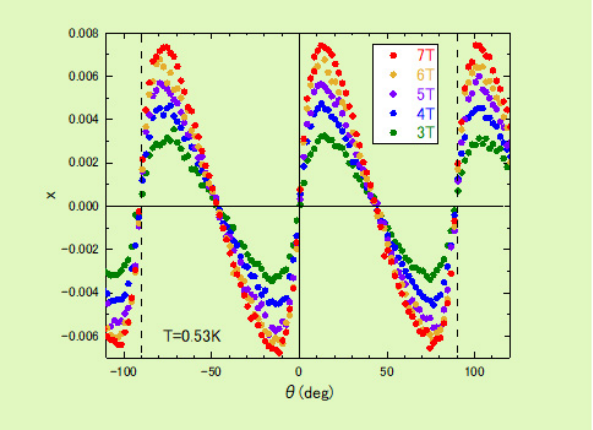

Fig. 2. Torque curves under various magnetic fields when the magnetic field was rotated in the ab plane at 0.53 K.

in Fig. 2. This feature is interpreted as the antiferromagnetism. The electrons responsible for these behavior should be *d* electrons of the Mn^{3}+ ion for the former case, and π electrons for the latter case. At first sight, it would be thought of that the electron we observe by our torque measurements might be the magnetic *d* electron only, in whichever plane the magnetic field was rotated. However, our former studies have already clarified that although the anisotropic one-dimensional Heisenberg (AODH) model which should describe only the behavior of the *d* electron can reproduce the feature of the torque signal with the magnetic field rotated in the plane including the *c*-axis, it is insufficient to describe the behavior of the torque when the magnetic field is rotated in the *ab* plane, in terms of the AODH model only. This model should be supplemented by the antiferromagnetic model of π electrons, because otherwise the behavior of torque signals in this field rotation plane cannot be reproduced at the region of low temperatures and low magnetic fields. We are thus allowed to consider that the electron we can observe when the field rotated in the *ab* plane should be the π electron, that is different from the electron when the field rotated in the plane including the *c*-axis. We are thus able to separate contributions due to the *d* and π electrons.

Now we also have to take the susceptibility data into account. That shows the weak antiferromagnetic behavior of the *d* electron as a result of applying the Curie-Weiss law. We have to reconcile the torque and the susceptibility data. One possibility is that the *d* electron should be in the canted antiferromagnetic state, instead of the ferromagnetic. Even in the canted antiferromagnetic case, the torque curve is also the same as that in the ferromagnetic case if the anisotropy energy is very small. We also pointed out that the experimental observation that the magnetoresistance is hardly seen is consistent with the canted antiferromagnetic model. The canted antiferromagnetism is very likely, because the canted antiferromagnetism might be mediated by the Dzyaloshinsky-Moriya interaction. In fact, the space inversion symmetry is broken and the spin-orbit coupling plays an important role in our sample.

Reference
[1] K. Torizuka, Y. Uwatoko, M. Matsuda, G. Yoshida, M. Kimata, and H. Tajima, J. Phys. Soc. Jpn. **86**, 114709 (2017).

Authors
K. Torizuka[a], M.Matsuda[b], and Y. Uwatoko
[a]Nippon Institute of Technology
[b]Kumamoto University

Identification of the Key Interactions in Structural Transition Pathway of FtsZ from Staphylococcus Aureus

Y. Shigeta, R. Harada, and H. Matsumura

The bacterial cell division protein FtsZ forms a ring-shaped filament (Z-ring) inside the cell membrane in the presence of GTP, and dynamically repeats division and dissolution owing to treadmilling coupled with the GTPase activity to cause invagination of the cell membrane. Although this invagination is thought to be caused by shrinking of the Z-ring, its molecular mechanism is still unknown. The crystal structure of GDP-bound *Staphylococcus aureus* FtsZ (SaFtsZ-GDP complex) was experimentally determined by X-ray structural analysis. Surprisingly, there are two different

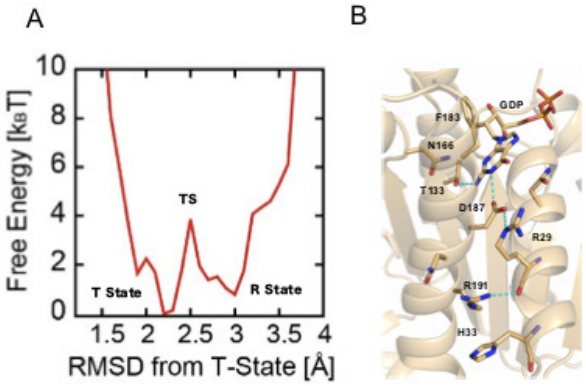

Fig. 1. (A)Free energy landscape of SaFtsZ, which connects T- and R-state. (B) Transition state structure during T- and R-state transition around GDP binding site.

three-dimensional structures in the same crystal, which correspond to GTP- and GDP-bound forms (or tense (T) and relaxed (R) states) in the other species. Visualization of the two states in the same species enables us to investigate the structural transition pathway between the T and R states, which might be related to the constriction of the Z-ring. Generally, in order to reproduce large-scale structural transitions related to biological functions *in silico*, extremely long-time molecular dynamics (MD) simulation is required. To avoid this problem, it is necessary to apply some structure sampling method in order to reproduce important structural changes efficiently as quickly as possible. In this research, we apply parallel cascade selection MD (PaCS-MD) simulation developed by us [1, 2] for searching structural transition pathways between the T and R states [3]. After obtaining the transition pathway we have evaluated free energy landscape (FEL) and find transition state (TS) structure (see Fig. 1). From the FEL, the free energy difference and barrier between the two states are merely k_BT and $4k_BT$, respectively, indicating the monomeric SaFtsZ-GDP complex exists in equilibrium. During the transition, it is found that the main chain carbonyl group of Arg29, whose side chain moves significantly between the T and R states, tentatively forms a hydrogen bond with Arg191 nearby in the TS. From these analysis, it is found that Arg29 is a key amino acid residue for the function of FtsZ, and a subsequent mutagenesis work also support the hypothesis.

References
[1] R. Harada, and A. Kitao, J. Chem. Phys. **139**, 035103 (2013).
[2] R. Harada, Y. Takano, T. Baba, and Y. Shigeta, Phys. Chem. Chem. Phys. (feature article) **17**, 6155 (2015).
[3] J. Fujita, R. Harada, Y. Maeda, Y. Saito, E. Mizohata, T. Inoue, Y. Shigeta, H. Matsumura, J. Struct. Biol. **198**, 65 (2017).

Authors
J. Fujita[a], R. Harada[b], Y. Maeda[a], Y. Saito[a], E. Mizohata[a], T. Inoue[a], Y. Shigeta[b], and H. Matsumura[c]
[a]Osaka University
[b]University of Tsukuba
[c]Ritsumeikan University

Neutron Spin Resonance in the 112-Type Iron-Based Superconductor

H. Luo, S. Li, and T. Masuda

In unconventional superconductors, the neutron spin resonance is a crucial evidence for spin fluctuation mediated superconductivity in the proximity of an antiferromagnetic

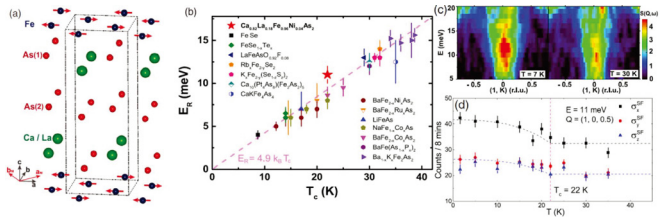

Fig. 1. (a) Crystal and magnetic structure of $Ca_{1-x}La_xFeAs_2$ system. (b) Linear scaling of spin resonance energy and critical temperature in Fe-based superconductors. (c) Spin resonance in superconducting 112 compound measured at HRC (BL-12). (d) Polarized analysis of spin resonance at E=11 meV.

(AF) instability [1]. Although the spin resonance mode is theoretically believed to be a spin-1 exciton from the singlet-triplet excitations of the electron Cooper pairs in copper oxides and heavy fermions[2], solid evidences are still not well established yet in the iron-based superconductors (FeSC). The proximity to the AF order and spin-orbital coupling give complexity on the energy and momentum distribution of spin resonance, and the common features of the resonance mode need to be testified in various materials[3].

By using inelastic neutron scattering, we have comprehensively studied the low-energy spin excitations of the new discovered 112-type iron pnictide $Ca_{0.82}La_{0.18}Fe_{0.96}Ni_{0.04}As_2$ with bulk superconductivity below T_c =22 K(Fig. 1(a)) [4]. A two-dimensional spin resonance mode is found around E =11 meV by using high-resolution chopper (HRC) spectrometer (Fig. 1(c)), where the resonance energy is almost temperature independent and linearly scales with T_c along with other iron-based superconductors (Fig. 1(b)). Polarized neutron analysis reveals the resonance is nearly isotropic in spin space without any L modulations (Fig. 1(d)). Because of the unique monoclinic structure with additional zigzag arsenic chains, the As 4p orbitals contribute to a three dimensional hole pocket around the Γ point and an extra electron pocket at the X point. Our results suggest that the energy and momentum distribution of the spin resonance does not directly respond to the k_z dependence of the fermiology, and the spin resonance intrinsically is a spin-1 mode from singlet-triplet excitations of the Cooper pairs in the case of weak spin-orbital coupling. This work is published on Physical Review Letters [5].

References

[1] P. Dai, Rev. Mod. Phys. **87**, 855 (2015).
[2] M. Eschrig, Adv. Phys. **55**, 47 (2006).
[3] P. D. Johnson, G. Xu, and W.-G. Yin, *Iron-Based Superconductivity* (Springer, New York, 2015).
[4] N. Katayama et al., J. Phys. Soc. Jpn. **82**, 123702 (2013).
[5] Tao Xie et al., Phys. Rev. Lett. **120**, 137001 (2018).

Authors
T. Xie[a,b], D. Gong[a,b], H. Ghosh[c,d], A. Ghosh[c,d], M. Soda, T. Masuda, S. Itoh[e], F. Bourdarot[f], L.-P. Regnault[g], S. Danilkin[h], S. Li[a,b,i], and H. Luo[a]
[a]Chinese Academy of Sciences
[b]University of Chinese Academy of Sciences
[c]Homi Bhabha National Institute
[d]Raja Ramanna Centre for Advanced Technology
[e]High Energy Accelerator Research Organization
[f]Université Grenoble Alpes
[g]Intitut Laue Langevin
[h]Australian Nuclear Science and Technology Organization
[i]Collaborative Innovation Center of Quantum Matter

Test of Vacuum Anisotropy under High Magnetic Fields: Vacuum Magnetic Birefringence Experiment

T. Inada, T. Yamazaki, and K. Kindo

Classical electrodynamics governed by Maxwell's equations describes the vacuum as an isotropic and dispersion-less medium, which properties are not affected by the application of electromagnetic fields. However, if we consider quantum electrodynamics (QED), the nonlinear interaction between the fields is mediated by the vacuum fluctuation of virtual particle-antiparticle pairs. Consequently, the vacuum shows a finite size of anisotropy under strong magnetic fields, called vacuum magnetic birefringence (VMB). In addition to this QED effect, VMB can be enhanced by the contribution from undiscovered particles such as axions, which are one of the leading candidates of dark matter. The test of VMB therefore provides one of the most sensitive searches for these particles with a mass around meV.

Three groups are currently trying to measure VMB, with a common scheme shown in Fig. 1. It consists of crossed-Nicols polarizers, a high-finesse Fabry-P´erot cavity, and a magnet that applies transverse fields with respect to the laser axis. The VMB signal is measured as ellipticity induced by the magnet. The surface of cavity mirrors has large static birefringence, and to separate the VMB signal from it, magnetic fields are temporally modulated. The modulation is realized by a rotating permanent magnet (~ 2.5 T) by one of the groups, whereas we instead use a pulsed magnet since the VMB signal is enhanced according to the square of the field strength (B^2). Our magnet produces alternative fields of +9 T and −4.5 T with a high repetition rate of 0.1 Hz [1, 2].

The sensitivity to VMB is determined by the background process of the Faraday effect caused by residual gas in the chamber. Since the Faraday component is linearly depends on B, we apply alternative fields to subtract it. To emulate the B^2 dependence of the small VMB signal, we first filled a relatively high pressure of nitrogen gas (100 Pa) and observed the square term of linear Faraday effect. Figure 2(a) shows the agreement of the measured B^2 term with calculation of the squared Faraday term. The VMB measurement was then carried out under vacuum with ~ 2000 cycles of the alternating fields in 2018. The VMB coeffcient k_{CM} is calculated for each cycle and distributed as shown in Fig. 2(b). The mean value of the distribution is consistent with zero, showing no sign of axionic contribution. As

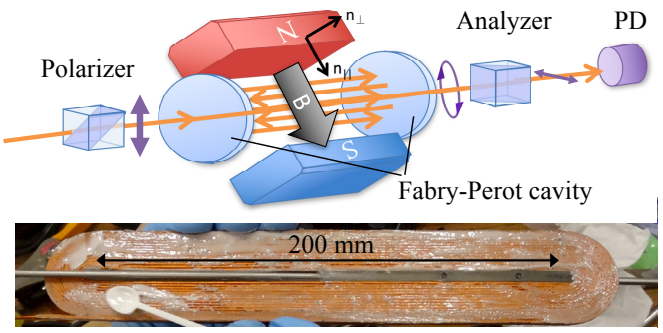

Fig. 1. (upper) Schematic veiw of the setup. An incident light is polarized and stored in a high-finesse Fabry-P´erot cavity, where pulsed magnetic fields induce elliptical polarization. (lower) Bare racetrack coil before backed up with an outer metal. The magnet produces fields of up to 10 T over the beam path.

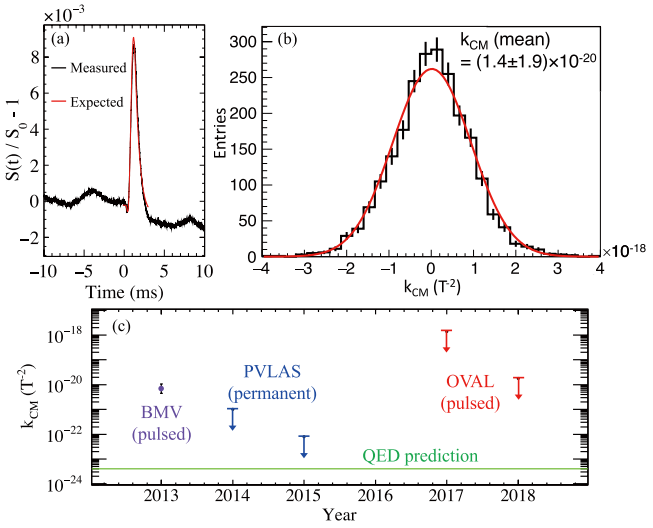

Fig. 2. (a) Test measurement of the small square term of the Faraday effect caused by 100 Pa of nitrogen gas, compared to calculation. The vertical axis shows the ratio of signal height with respect to the static component S_0. (b) Histogram of vacuum ellipticity coeffcient k_{CM} obtained by 2000 cycles of alternating +9 T and −4.5 T fields. The fitting to a Gaussian distribution shows a zero-consistent value for the mean, which gives an upper limit on k_{CM}. (c) Comparison of the current limits on k_{CM} (OVAL) with the other two groups. Note that, without hypothetical particles such as axions, QED alone predicts finite vacuum birefringence shown as the green line.

a result, it poses an upper limit on k_{CM}, that is plotted in Fig. 2(c) with recent results of the other groups. We have improved our first result in 2017 by two orders of magnitude [3]. There is still a large gap of sensitivity to reach the signal level predicted by QED, and upgrades on the magnet and optics are currently underway.

References

[1] T. Inada *et al*., Phys. Rev. Lett. **118**, 071803 (2017).
[2] T. Yamazaki *et al*., Nucl. Instrum. Methods Phys. Res. A **833**, 122 (2016).
[3] X. Fan *et al*., Eur. Phys. J. D **71**, 308 (2017).

Authors

T. Inada[a], T. Yamazaki[a], X. Fan[a], S. Kamioka[a], T. Namba[a], T. Kobayashi[a], S. Asai[a], J. Omachi[a], K. Yoshikawa[a], M. Kuwata-Gonokami[a], Y. Tamasaku[b], Y. Inubushi [b], K. Sawada[b], M. Yabashi[b], T. Ishikawa[b], Y. Tanaka[c], H. Nojiri[d], A. Matsuo, K. Kawaguchi, and K. Kindo

[a]The University of Tokyo
[b]RIKEN Spring-8
[c]University of Hyogo
[d]Tohoku University

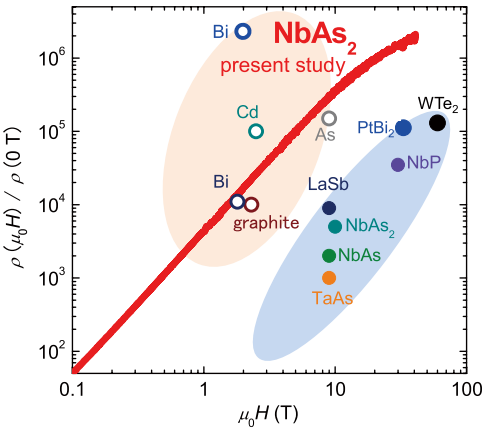

Fig. 1. Magnetoresistance in representative semimetals exhibiting large MR. Typical area of MR in elemental (open circles) and binary semimetal (closed circles) in the previous reports are shown by different colors.

a few tesla, resulting in the MR much larger than those recently reported for the binary systems. On the other hand, the binary semimetals tend to have lower carrier mobility. Thus, the increasing rate of MR is suppressed, resulting in a non-saturating MR with much smaller value in a reachable field. Therefore, it may be possible to enhance the MR in binary semimetals merely by improving the crystal quality.

In this study, we have synthesized high quality single crystals of $NbAs_2$ by the chemical vapor transport technique and observed an extremely large magnetoresistance exceeding 1.9 million at 1.7 K at 40 T. The present MR value is one or two orders of magnitude larger than that for the binary systems reported so far and reaches as high-level as that of the ultra-high mobility elemental semimetals. We showed that both of carrier mobility and charge compensation ratio were significantly improved in the present $NbAs_2$ crystal exhibiting mega-scale MR. Thus, we demonstrate that the binary semimetal has a great potential to exhibit further significant enhancement of MR merely by the improvement of the crystal quality.

Reference

[1] K. Yokoi, H. Murakawa, M. Komada, T. Kida, M. Hagiwara, H. Sakai, and N. Hanasaki, Physical Review Materials **2**, 024203 (2018).

Authors

K. Yokoi[a], H. Murakawa[a], M. Komada[a], T. Kida[a], M. Hagiwara[a], H. Sakai[a], and N. Hanasaki[a]

[a]Osaka University

Mega-Scale Magnetoresistance in the Binary Semimetal $NbAs_2$

H. Murakawa, K. Yokoi, and T. Kida

Recently, large magnetoresistance (MR) has been reported for a wide variety of binary semimetals. The MR values for these materials reaches 10^3 ~ 10^5 below 4 K without an indication of saturation even at several tens of tesla. Although, the MR in these binary semimetals are reported to be “extremely large”, these values have been far smaller than those in classical elemental semimetals such as bismuth reported 80 years ago. In general, magnetoresistance in a semimetal is simply explained by two carrier model, in which the carrier mobility is the decisive parameter for the MR value. In fact, for ultrahigh mobility elemental semimetals such as bismuth, the MR grows rapidly in only

Quantum Hall Effect in Topological Dirac Semimetal Cd_3As_2 Films

M. Uchida, M. Tokunaga, and M. Kawasaki

As crystalline materials of three-dimensional Dirac semimetal, Cd_3As_2 and Na_3Bi have been suggested, and their unique electronic structures have been directly observed through angle-resolved photoemission and scanning tunneling spectroscopy. On the other hand, its quantum transport especially at high fields has been still elusive, because fabrication of high-quality Dirac semimetal films has been highly challenging unlike other topological materials. While Cd_3As_2 has long been known as a stable II–V type semiconductor, its film quality has been limited due to the necessity of low-temperature growth.

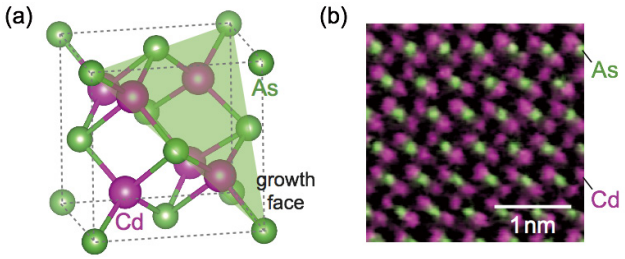

Fig. 1. (a) Primary crystal structure of topological Dirac semimetal Cd_3As_2. (b) Cross-sectional transmission electron microscopy image of a Cd_3As_2 film fabricated by high-temperature annealing. Cd and As atoms are periodically arranged without any clear crystallographic defects over a wide area.

Here we report the observation quantum Hall effect and its thickness dependence by measuring high-quality Cd_3As_2 films fabricated by high-temperature annealing (Fig. 1) [1, 2]. Transport measurements up to 55 T were performed using a nondestructive pulse magnet with a pulse duration of 37 ms. Longitudinal resistance R_{xx} and Hall resistance R_{yx} were measured on the 60 μm-width Hall bar with flowing a DC current of $I = 5$ μA.

Figure 2 shows high-field magnetotransport for two Cd_3As_2 films with the same carrier density ($n = 1 \times 10^{18}$ cm^{-3}) and different thicknesses (t = 12 and 23 nm). Shubnikov-de Haas (SdH) oscillations and plateau-like structures are resolved in longitudinal resistance R_{xx} and Hall resistance R_{yx}. As the field increases, integer quantum Hall states appear down to the quantum limit of filling factor $\nu = 2$. R_{xx} finally becomes zero, and simultaneously, R_{yx} shows quantized values over wide field ranges. Temperature dependence of R_{xx} measured from 1.4 to 50 K can be well fitted with the standard Arrhenius plot, giving high activation energy of $\Delta = 19$ K ascribed to the unusually high Fermi velocity in the Dirac semimetal. Absence of the half-integer plateaus suggests that a gap starts to open under the quantum confinement to the Dirac semimetal state. Furthermore, the degeneracy factor shows an interesting change depending on the film thickness; It is altered from 2 to 1 with increase of film thickness. Detailed analysis reveals that this change is attributed to spin splitting or g factor change, not to the lifting of other degeneracies, e.g., of valley or surface states.

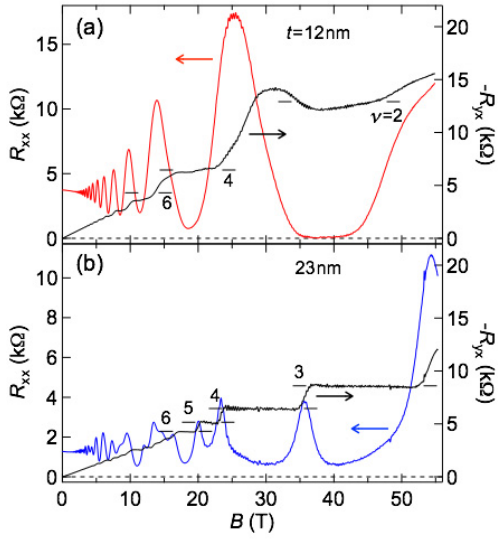

Fig. 2. (a) High-field magnetotransport for a relatively thin Cd_3As_2 film (t = 12 nm) measured at T = 1.4 K. The numbers of the horizontal bars represent the filling factor ν, determining the degeneracy factor to be 2 from its increment. (b) Same scan for slightly thicker films (t = 23 nm). By contrast, the degeneracy is altered to 1 in this thicker film at high fields.

Reflecting the high Fermi velocity of the Dirac dispersion, the band gap sharply opens when the confinement thickness, giving rise to the drastic change of the g factor change observed in the quantum Hall effect.

Detailed electronic structures including subband splitting and gap opening are determined by analyzing the quantum transport depending on the confinement thickness. The demonstration of quantum Hall states in the high-quality Cd_3As_2 films opens a road to study high-field quantum transport in topological Dirac semimetal and its derivative phases. Combining electric gating, heterostructure fabrication, or chemical doping techniques to the high-field measurements will open possibilities for further studying quantized transport phenomena by tuning Fermi level, hybridization gap, or magnetic interaction.

References

[1] M. Uchida, Y. Nakazawa, S. Nishihaya, K. Akiba, M. Kriener, Y. Kozuka, A. Miyake, Y. Taguchi, M. Tokunaga, N. Nagaosa, Y. Tokura, and M. Kawasaki, Nature Communications **8**, 2274 (2017).
[2] Y. Nakazawa, M. Uchida, S. Nishihaya, M. Kriener, Y. Kozuka, Y. Taguchi, and M. Kawasaki, Scientific Reports **8**, 2244 (2018).

Authors
M. Uchida[a], M. Tokunaga, and M. Kawasaki[a]
[a]The University of Tokyo

Robustness of Emergent Monopole Fluctuations in a Chiral Magnet MnGe under High Magnetic Fields

N. Kanazawa, Y. Tokura, and M. Tokunaga

Topological spin textures are a fertile source of emergent electromagnetic responses owing to their quantized Berry phase. Berry phase acts as a fictitious magnetic flux, so-called an emergent magnetic flux, affecting the motion of conduction electrons in solids. By designing a topological spin arrangement, we can achieve an arbitrary emergent magnetic field distribution, whose magnitude may reach as large as 4000 T when the size of topological spin object is squeezed in 1-nm^2 area. In addition to such possible gigantic electromagnetic responses, it is also noteworthy that we can effectively realize the magnetic monopole structures, where the magnetic field distribution is inversely proportional to the square of the distance ($\propto \boldsymbol{r}/|\boldsymbol{r}|^3$).

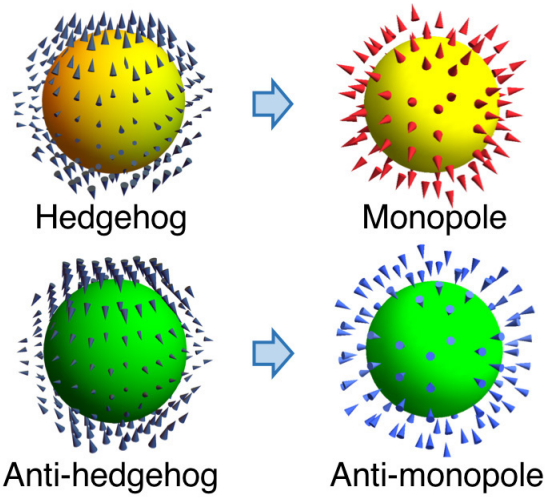

Fig. 1. Spin hedgehogs and corresponding monopole-type emergent field distributions.

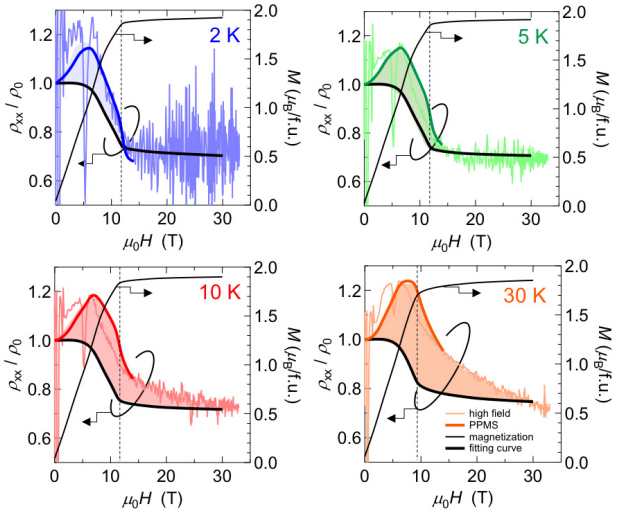

Fig. 2. Longitudinal magneto-resistivity (MR) measured with use of mid-pulse magnet at low temperatures (T = 2, 5, 10, 30 K). Thick-line curves are the results obtained by steady-field measurements (PPMS) up to 14 T. Bold black curves are the estimated conventional MR associated with the variations of magnetization shown in the black thin lines.

In a chiral magnet MnGe, there realized three-dimensional hairy spin structures, so-called spin hedgehogs, which behave as the quantized sources or sinks of effective gauge field, that is, emergent monopoles and anti-monopoles (Fig. 1). In association with emergent-monopole motion driven by an external magnetic field, dramatic changes in magneto-transport properties appear, exhibiting unusual magnetic-field dependence, such as positive magneto-resistance, multiple elastic anomalies, magnetic-field-enhanced thermopower and so on [1]. Those unusual properties are rooted in large fluctuations of emergent monopoles, which induce considerable dynamical variations in the emergent magnetic field distribution and consequently cause intense scatterings of electrons, phonons and magnons.

By high-field measurements of magnetization and resistivity with use of the mid-pulse magnets installed at ISSP, we experimentally found that the emergent monopole fluctuations can survive far beyond the topological transition where the majority of spin hedgehogs undergo pair annihilation [2]. Figure 2 shows the magnetic field dependence of magnetization (M) and magneto-resistivity normalized by its zero-field value (ρ_{xx}/ρ_0). We compare the measured ρ_{xx}/ρ_0 (color lines in Fig. 2) with the ordinary contribution to ρ_{xx}/ρ_0 from the alignment of spins (thicker black lines, estimations from the M-profiles), so as to evaluate the unusual contribution from the monopole fluctuations (color shades). While at the low temperatures (T = 2 K and 5 K) the unusual contribution only exists below the magnetic field H_c with the topological transition (vertical dashed lines), it persists even above H_c only with small temperature elevation above 10 K. This result may indicate the possibility that a part of spin hedgehogs escaping from their annihilation or thermally excited hedgehog-like spin structure may exist even in the high-field regime and their fluctuations cause strong scatterings of charge carriers. The observed robustness of the emergent monopole fluctuations possibly originates from topological protection against unwinding of the spin texture by external magnetic fields.

The present results not only open the door to veiled characteristic properties of emergent monopoles in the high-field regime but also demonstrate promising usefulness of high-field measurements to clarify the topological stability of spin nano-objects.

References

[1] N. Kanazawa, Y. Nii, X.-X. Zhang, A. S. Mishchenko, G. De Filippis, F. Kagawa, Y. Iwasa, N. Nagaosa, and Y. Tokura, Nature Commun. **7**, 11622 (2016).

[2] Y. Fujishiro, N. Kanazawa, T. Shimojima, A. Nakamura, K. Ishizaka, T. Koretsune, R. Arita, A. Miyake, H. Mitamura, K. Akiba, M. Tokunaga, J. Shiogai, S. Kimura, S. Awaji, A. Tsukazaki, A. Kikkawa, Y. Taguchi, and Y. Tokura, Nature Commun. **9**, 408 (2018).

Authors

Y. Fujishiro[a], N. Kanazawa[a], T. Shimojima[b], A. Nakamura[a], K. Ishizaka[a,b], T. Koretsune[b], R. Arita[b], A. Miyake, H. Mitamura, K. Akiba, M. Tokunaga, J. Shiogai[c], S. Kimura[c], S. Awaji[c], A. Tsukazaki[c], A. Kikkawa[b], Y. Taguchi[b], and Y. Tokura[a,b]

[a]The University of Tokyo

[b]RIKEN Center for Emergent Matter Science (CEMS)

[c]Tohoku University

Magnetization Process of the S = 1/2 Two-Leg Organic Spin-Ladder Compound BIP-BNO

Y. Hosokoshi, S. Todo, and Y. H. Matsuda

Spin-ladder systems are a class of low-dimensional materials that correspond to the crossover region between one and two dimensions. The quantum-mechanical properties and criticality of spin-ladder systems have attracted considerable attention. In the S = 1/2 spin-ladder system with the antiferromagnetic Heisenberg (AFH) exchange interaction, it is theoretically predicted that the even-leg spin ladder has a spin gap, while the odd-leg spin ladder is gapless [1, 2]. The spin states of the even-leg AFH spin ladders in the presence of a magnetic field (B) are particularly interesting. There is a transition to a gapless Tomonaga-Luttinger liquid (TLL) phase at a critical magnetic field (B_{c1}) from a gapped disordered spin liquid state. The quantum critical phenomena are observed in the vicinity of B_{c1} as well as another critical field B_{c2} at which the spins are fully polarized [3, 4].

BIP-BNO (3,5'-bis(N-tert-butylaminoxyl)-3',5-dibromobiphenyl, $C_{20}H_{24}N_2O_2Br_2$) is a candidate for an S = 1/2 two-leg spin-ladder in which there are no transition metal element but NO groups have S = 1/2 spins [5]. However, since the susceptibility is well reproduced by both a spin-ladder model and a bond-alternating chain model, the key to identify BIP-BNO as a spin-ladder is the magnetization (M)

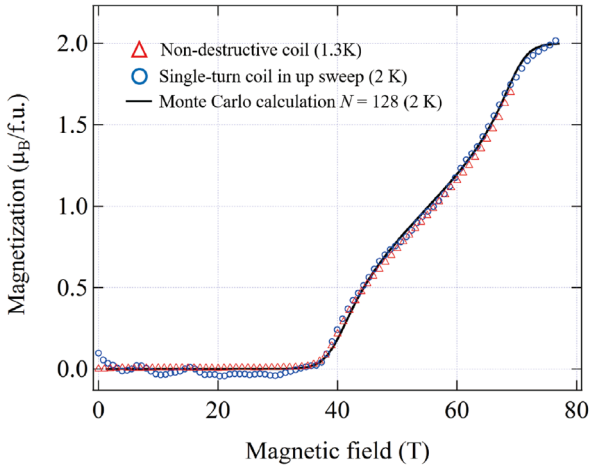

Fig. 1. Magnetization curve of BIP-BNO. The circles and triangles represent the experimental results of the single turn coil and the non-destructive coil, respectively. The solid line shows the numerical result calculated by the quantum Monte Carlo method.

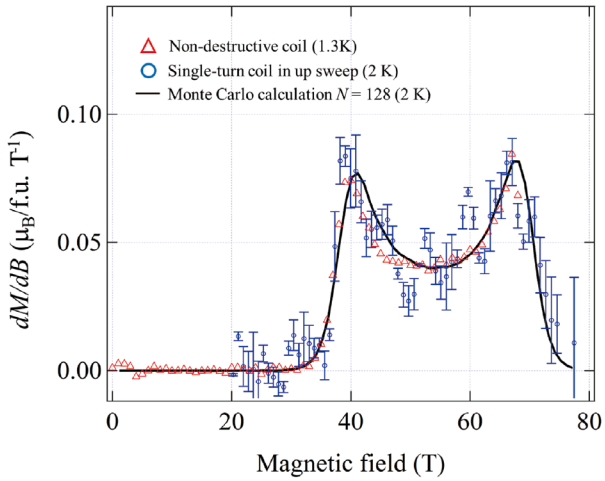

Fig. 2. Magnetic field derivative of magnetization. The solid line, circles, and triangles represent the numerical calculation, experimental result with VSTC, and that with MLPM, respectively. The error bars represent the statistical errors of the experiments of VSTC.

process. In the previous study, the magnetization curve up to 50 T clearly shows the transition at around 35 T. However, the observed magnetization is approximately only up to a quarter of the saturation value M_{sat} = 2 μB/f.u. To clarify the property of BIP-BNO as a spin-ladder system and to determine accurate exchange constants, it is required to analyze the full magnetization curve and see how well the ladder model can explain the experimental observations.

The measured magnetization curves at low temperatures (1.3 and 2 K) are shown in Fig. 1. The result obtained from a non-destructive-type multilayer-pulsed magnet (MLPM) and that from the destructive-type vertical single-turn coil (VSTC) are represented by triangles and the circles, respectively. Although the pulse duration of VSTC is three orders of magnitude shorter than that of MLPM, the obtained two magnetization curves are found to be almost identical in the field range up to 70 T, which suggests an accurate measurement was conducted not only with non-destructive MLPM but also the destructive VSTC. The magnetization below 37 T is nearly zero reflecting the spin-liquid ground state, which is consistent with the previous study. It is found that the magnetization suddenly starts increasing at 37 T and shows the saturation at fields exceeding 74 T. We expect that the phase in the region where the magnetization is larger than zero and smaller than the saturation value should be the TLL as it is suggested in other two-leg spin-ladder materials. Hence, we find B_{c1} = 37 T and B_{c2} = 74 T. To compare experimental data with the theoretical model, we calculated the magnetization of the spin-ladder system under a magnetic field by means of the worldline quantum Monte Carlo method with the worm (directed-loop) algorithm. The worm scattering probability is optimized using the geometric allocation. The exchange constants of the model are estimated using the simulated annealing in which the deviation from the experimentally obtained magnetization curve is minimized. The calculated magnetization curve (solid line) is shown in Fig. 1 and we obtain J_{rung}/k_B = 65.7 K and J_{leg}/k_B =14.1 K, where J_{rung} and J_{leg} are the exchange constants for the leg and rung directions of the ladder, respectively.

Figure 2 represents *dM/dB* as a function of *B*. Sharp two peaks are clearly seen in the numerically calculated as well as experimentally obtained *dM/dB* curves. Moreover, the inflection point between the two peaks is found to be located at approximately 55 T where $M = M_{sat}/2$, and the symmetric form with respect to the inflection point is clearly seen. The symmetric shape in *dM/dB* is the specific character of a spin-ladder [6]. It should be noted that a bond-alternating chain also give two peaks in the *dM/dB* curve. However, the shape is distinctly asymmetric; the peak heights of the two are different, e.g., the height of the lower-field peak is from 20 % to 70 % of the height of the higher-field peak, depending on the alternation parameter. Moreover, the inflection point between the two peaks is not at the center position. The difference between the heights of the two peaks in BIP-BNO is evaluated to be only 3% in *dM/dB* and the inflection point located at the center between the two peaks, which cannot be attributed to a bond-alternating chain. These findings provide strong evidence that BIP-BNO is identified with the S = 1/2 two-leg spin ladder [7].

The ratio of the Heisenberg exchange constants J_{rung}/J_{leg} is estimated to be approximately 4.7, which is deeply in the strong coupling region: $J_{rung}/J_{leg} > 1$. In the curve of the magnetic-field derivative of the magnetization, dM/dB, the characteristic features, namely two sharp peaks and a centered inflection point, are observed with a symmetric shape. This observation strongly suggests that BIP-BNO is an S = 1/2 AFH two-leg spin ladder. It is worth noting that BIP-BNO is the first prototypical organic (not containing magnetic ions) S = 1/2 spin-ladder compound.

References
[1] E. Dagotto, J. Riera, and D. Scalapino, Phys. Rev. B **45**, 5744 (1994).
[2] M. Azuma, Z. Hiroi, and M. Takano, Phys. Rev. Lett. **73**, 3463 (1994).
[3] S. Sachdev, Science **288**, 475 (2000).
[4] B. C. Watson, V. N. Kotov and M. W. Meisel *et al.,* Phys. Rev. Lett. **86**, 5168 (2001).
[5] K. Katoh, Y. Hosokoshi, and K. Inoue *et al.*, J. Phys. Chem. Solids **63**, 1277 (2002).
[6] X. Wang and L. Yu, Phys. Rev. Lett. **84**, 5399 (2000).
[7] K. Nomura, Y. H. Matsuda, and Y. Narumi *et al.,* J. Phys. Soc. Jpn. **86**, 104713 (2017).

Authors
K. Nomura, Y. H. Matsuda, Y. Narumi[a], K. Kindo, S. Takeyama, Y. Hosokoshi[b], T. Ono[b], N. Hasegawa[b], H. Suwa[c], and S. Todo[c]
[a]Osaka University
[b]Osaka Prefecture University
[c]The University of Tokyo

Convergence of the Magnetic Grüneisen Parameter at the Quantum Critical Point of the Transverse-Field Ising-Chain

Z. Wang and Y. Kohama

Quantum critical point (QCP) is the end point in a phase diagram where a continuous phase transition occurs at absolute zero temperature. So far, a lot of efforts have been made to understand the universal scaling behavior in different types of QCPs. In case of field-induced QCP, heavy-fermion compound and one-dimensional Heisenberg spin systems are known to show a divergence in thermodynamically properties, such as specific heat and magnetic Grüneisen parameter (Γ_m). In contrast, for the QCP of the transverse-field Ising (TFI) spin chain system, it is theoretically shown that the Γ_m does not show a divergence behavior when the QCP is approached by decreasing temperature at the critical field, although it diverges when the critical field is approached at zero temperature [1]. While many theoretical works on the TFI spin chain system are now available, it remains very challenging to experimentally realize the

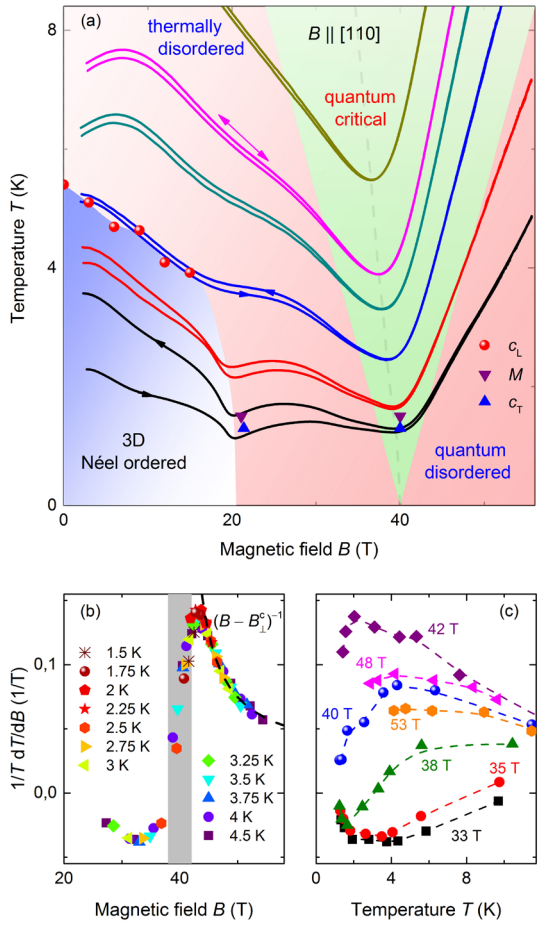

Fig. 1. (a) Magnetocaloric-effect in $BaCo_2V_2O_8$. The magnetic field was applied to the [110] direction. (b), (c) The estimated Grüneisen parameter, $\frac{1}{T}\frac{dT}{dB}$, as a function of magnetic field and temperature.

paradigmatic model in a real material.

In our recent work [2], we show that the Ising-like spin-1/2 antiferromagnetic chain material $BaCo_2V_2O_8$ exhibits the unique QCP behavior of the TFI spin system which fulfills the requirements of its experimental observations; (1) strong easy axis anisotropy (2) negligible inter-chain coupling, (3) accessible critical field strength of ~40 T. In this research, we have performed magnetization, sound velocity, and magnetocaloric-effect measurements as a function of temperature and transverse magnetic field on the single crystal of $BaCo_2V_2O_8$, and have provided the experimental evidence of convergence behavior in Γ_m. To the best of our knowledge, the Γ_m above 20 T has been experimentally obtained for the first time in this research, by using the pulsed field magnetocaloric effect (MCE) measurement.

Figure 1(a) shows the magnetocaloric effect data up to 55 T for various initial temperatures. The field dependence of the sample temperature, $T(B)$, detects the 3D Néel ordered phase at about 20 T and the field-induced QCP at 40 T as a broad minimum. The hysteresis below the critical field can be due to slow dynamical process such as field-driven reorientation of twin-domains as reported before. Figure 1(b) and (c) show the temperature and field dependences of $\frac{1}{T}\frac{dT}{dB}$. Since the $T(B)$ curves was obtained in an approximate adiabatic condition (the sample is thermally isolated due to the extremely short time scale of the pulsed field duration), the process can be considered as an isentropic one. Moreover, the lattice specific heat is not expected to be field dependent. Therefore, the obtained field dependent behavior of $\frac{1}{T}\frac{dT}{dB}$ corresponds to the $\Gamma_m = \frac{1}{T}\frac{dT}{dB}\Big|_S$. As seen in Fig. 1(b) the field dependence of $\frac{1}{T}\frac{dT}{dB}$ shows a divergence behavior approaching ~40 T. On the other hand, the temperature dependence of $\frac{1}{T}\frac{dT}{dB}$ does show a converging behavior at ~40 T with decreasing temperature (Fig. 1(c)). This is consistent with the previous theoretical prediction [1] and the first experimental observation of the characteristic scaling feature in the TFI-chain QCP [2].

References

[1] J. Wu, L. Zhu, and Q. Si, arXiv:1802.05627 (2018).

[2] Zhe Wang, T. Lorenz, D. I. Gorbunov, P. T. Cong, Y. Kohama, S. Niesen, O. Breunig, J. Engelmayer, A. Herman, Jianda Wu, K. Kindo, J. Wosnitza, S. Zherlitsyn, and A. Loidl, Phys. Rev. Lett. **120**, 207205 (2018).

Authors

Zhe Wang[a,b], T. Lorenz[c], D. I. Gorbunov[d], P. T. Cong[d], Y. Kohama, S. Niesen[c], O. Breunig[c], J. Engelmayer[c], A. Herman[c], J. Wu[e], K. Kindo, J. Wosnitza[d], S. Zherlitsyn[d], and A. Loidl[a]

[a]Experimental Physics V, Center for Electronic Correlations and Magnetism

[b]Institute of Radiation Physics, Helmholtz-zentrum Dresden-Rossendorf

[c]Institute of Physics II, University of Cologne

[d]Dresden High Magnetic Field Laboratory (HLD-EMFL), Helmholtz-Zentrum Dresden-Rossendorf

[e]Max-Plank-Institute für Physik komplexer Systeme

A Linear Correlation between Photocatalytic Activity and Photoexcited Carrier Lifetime

K. Ozawa, S. Yamamoto, and I. Matsuda

Laser-assisted time-resolved (TR) measurement techniques have facilitated great advances in our understanding of excited charge carrier dynamics. Preceding TR experiments have revealed many aspects of photocatalytic properties of TiO_2. One of them is that a higher photocatalytic activity of anatase TiO_2 (a-TiO_2) than rutile TiO_2 (r-TiO_2) results from a longer lifetime of the photoexcited carriers, owing to the different bulk band gap type (direct versus indirect types). On the other hand, it has also been recognized that the TiO_2 photocatalytic activity depends on the orientation of the crystal surfaces. Although several mechanisms such as a surface-dependent redox potential, anisotropic diffusion of the carriers, electron-trapping probability, etc. have been proposed as a possible origin, none of them comprehensively explains the surface dependence. Thus, a more detailed picture of the relation between the carrier dynamics and the photocatalytic activity must be drawn to understand the unique phenomenon.

In the present study, we systematically assessed the photocatalytic activities and photoexcited carrier lifetime on single-crystal a-TiO_2(101) and (001) surfaces and r-TiO_2(110), (001), (011), and (100) surfaces by X-ray photoelectron spectroscopy (XPS) and TR-XPS [1]. The photocatalytic activity was evaluated by a rate constant of a photocatalytic decomposition of acetic acid. The carrier lifetime was determined from a time evaluation of the ultraviolet (UV)-induced surface photovoltage (SPV).

Acetic acid adsorbs dissociatively on the TiO_2 surfaces via bonding interaction between the O atoms of carboxylate and the surface Ti atoms. Saturation coverages depend on

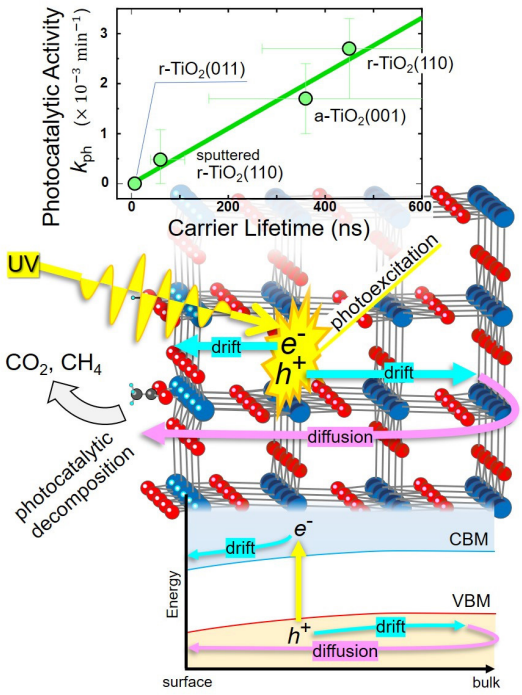

Fig. 1. Correlation between the photocatalytic activity and the carrier lifetime (top). Schematic illustrations of the photoexcited carrier dynamics in a real space (middle) and an energy space (bottom).

the surface orientation, but it ranges from 0.41 monolayers [on r-TiO$_2$(011)] to 0.66 monolayers [on r-TiO$_2$(100)]. The rate of the photocatalytic decompostion of acetic acid was estimated from a decreasing rate of the C 1s peak intensity while the UV laser with the energy of 3.31 eV was irradiated. The peak intensity decreases exponentially with a time constant τ_{ph} of 370 min on r-TiO$_2$(110). Since the reciprocal of τ_{ph} is a rate constant k_{ph}, k_{ph} on r-TiO$_2$(110) is evaluated to be 2.7×10^{-3} min^{-1}. This is the largest rete constant among all surfaces examined in the present study. k_{ph} on a-TiO$_2$(101) and (001) are 2.1×10^{-3} min^{-1} and 1.7×10^{-3} min^{-1}, respectively, while r-TiO$_2$(011) and (001) are inactive with $k_{ph} = 0$ min^{-1}.

The lifetime of the photoexcited carriers was determined from the time evolution of the SPV-induced Ti 2p peak shift. All TiO$_2$ surfaces examined in the present study form an accumulation layer at the surface because of the inevitable formation of surface oxygen vacancies. The SPV is generated on these surfaces by charge separation of the photexcited electron-hole pairs as illustrated in Fig. 1 (middle and bottom); the electrons and the holes are drifted towards the surface and bulk sides, respectively, along the potential gradient in the accumulation layer. The holes, then, diffuse back to the surface and recombine with the electrons at the surface. This charge separation-recombination process is the origin of the SPV generation-decay process. By examining the SPV decay time after the swift generation by TRXPS, the photoexcited carrier lifetime can be estimated. We examined the carrier lifetimes on three pristine surfaces [r-TiO$_2$(110), r-TiO$_2$(011), and a-TiO$_2$(001)] and one defective r-TiO$_2$(110) surface [2]. It is known that the lifetime strongly depends on the surface barrier height. Thus, the experimentally determined lifetimes were converted to barrier-height-corrected lifetimes so as to reproduce the lifetimes on the acetate-saturated surfaces; they are 450 ns, 360 ns, and 7 ns for r-TiO$_2$(110), a-TiO$_2$(001), and r-TiO$_2$(011), respectively.

The lifetime is found to be proportional to k_{ph}. A plot of k_{ph} against the lifetime gives a linear and positive correlation (top of Fig. 1). The linear correlation is extendable even to the sputtered surface [1]. On the other hand, no such correlation is found between k_{ph} and the surface chemical reactivity, which should be related to the saturation coverage of acetic acid. The photocatalytic reaction is initiated by an interaction between adsorbates and photoexcited carriers at the surface. The present study indicates that the carrier density on the surface rather than the adsorbate density is a prime factor to determine the photocatalytic activity, since more carriers are available for the reaction when the carriers survive longer. Thus, the carrier lifetime is a key to understand various properties of TiO$_2$ photocatalysis, including the orientation-dependent activity.

References

[1] K. Ozawa, S. Yamamoto, R. Yukawa, R.-Y. Liu, N. Terashima, Y. Natsui, H. Kato, K. Mase, and I. Matsuda, J. Chem. Phys. C **122**, 9562 (2018).
[2] K. Ozawa, S. Yamamoto, R. Yukawa, R. Liu, M. Emori, K. Inoue, T. Higuchi, H. Sakama, K. Mase, and I. Matsuda, J. Chem. Phys. C **120**, 29283 (2016).

Authors

K. Ozawa[a], S. Yamamoto, R. Yukawa[b], R.-Y. Liu[c], N. Terashima[d], Y. Natsui[d], H. Kato[d], K. Mase[b], and I. Matsuda
[a]Tokyo Institute of Technology
[b]Institute of Materials Structure Science, High Energy Accelerator Research Organization (KEK)
[c]Institute of Physics, Academia Sinica
[d]Hirosaki University